JOURNAL OF GEOPHYSICAL RESEARCH, VOL. 102, NO. B12, PAGES 27,319-27,340, DECEMBER 10, 1997

Seismic structure and indicators of magma budget along the Southern East Pacific Rise

Emilie E. E. Hooft,[1] Robert S. Detrick, and Graham M. Kent[2]

Department of Geology and Geophysics, Woods Hole Oceanographic Institution, Woods Hole, Massachusetts

Abstract. In this paper we re-examine the relationship between seismically constrained variations in crustal structure along the southern East Pacific Rise (SEPR) and the segment-scale variations in axial depth, morphology, basalt geochemistry, and hydrothermal activity that have often been attributed to along-axis differences in the supply of magma to the mid-ocean ridge. Along >800 km of the fast spreading SEPR, good correlations exist between axial depth, ridge cross-sectional area, mantle Bouguer anomaly, and the MgO weight percent of basalts recovered from the rise axis. These correlations indicate along-axis changes in crustal thickness and temperature consistent with variations in magma supply on time scales of ~100,000 years. In contrast, we show that the depth and width of the midcrustal magma sill, the thickness of seismic layer 2A, and the intensity of hydrothermal venting are poorly correlated with regional variations in ridge depth and cross-sectional area. We suggest that the emplacement geometry (width of the intrusion zone and flow lengths), not magma supply, controls extrusive layer (seismic layer 2A) thickness. We hypothesize that magma lens properties and hydrothermal activity are closely linked to spreading events (dike intrusion, eruptions, faulting) which occur on much shorter timescales (~10-100 years) than the longer-term variations in magma supply reflected in along-axis changes in the shape and depth of the ridge axis.

1. Introduction

Over the past decade, work on the fast spreading East Pacific Rise (EPR) has shown the existence of significant, segment-scale variations in axial depth [*Macdonald et al.*, 1984; *Macdonald and Fox*, 1988], axial volume [*Scheirer and Macdonald*, 1993], axial gravity anomaly [*Madsen et al.*, 1990; *Magde et al.*, 1995], magma chamber depth and width [*Detrick et al.*, 1987; *Kent et al.*, 1990; *Detrick et al.*, 1993], basalt geochemistry [*Langmuir et al.*, 1986; *Sinton et al.*, 1991; *Mahoney et al.*, 1994], and hydrothermal activity [*Haymon et al.*, 1991; *Baker*, 1996]. This along-axis variability in ridge crest observables has often been attributed to differences in magma supply to the ridge within or between segments [*Macdonald et al.*, 1984; *Macdonald and Fox*, 1988; *Macdonald et al.*, 1992] and is largely independent of spreading rate. Broad, shallow sections of ridge are assumed to reflect a high magma supply and are predicted to have larger, more robust axial magma chambers, erupt more primitive basalts, form thicker crust, have an axial summit caldera (ASC), and have more vigorous hydrothermal circulation than sections on the EPR with a deeper, narrower rise crest (Figure 1). In this context, magma supply is the time-averaged flux of melt from the mantle to the crust at the ridge axis. Provided that there is no strong along-axis transport of melt at crustal levels, seismic crustal thickness is one of the most direct measures of ridge crest magma supply. We use the term indicators of ridge magma supply to mean those other geological, geochemical, and geophysical observables (e.g. axial depth and volume, magma chamber depth and width, basalt geochemistry, and hydrothermal activity) that may reflect the magmatic state of the ridge crest. In this paper we quantitatively examine the relationship among various indicators of ridge magma supply to better understand the processes controlling the formation and evolution of the ridge axis.

There is evidence both in support of, and against, a simple magma supply model as is illustrated in Figure 1. The strongest evidence supporting this model has come from the systematic, segment-scale variations in axial depth and morphology observed along the EPR [*Macdonald et al.*, 1984; *Macdonald and Fox*, 1988; *Lonsdale*, 1989b; *Scheirer and Macdonald*, 1993] and the apparent correlation of these variations with the presence or absence of a reflection from a midcrustal magma sill [*Detrick et al.*, 1987; *Harding et al.*, 1989; *Kent et al.*, 1990; *Detrick et al.*, 1993]. The axial high at the EPR is typically shallowest near the middle of segments and deepens significantly toward segment offsets [*Macdonald et al.*, 1984; *Lonsdale*, 1989b]. These variations in axial depth are associated with systematic changes in the shape of the axial high [*Macdonald and Fox*, 1988; *Scheirer and Macdonald*, 1993]. Where the ridge is shallowest the axial high generally has a broad, flat-topped crosssection, where the ridge axis is deeper the axial high usually has a narrow, triangular shape. Based on this morphological evidence, *Macdonald et al.* [1984] and *Macdonald and Fox* [1988] suggest that the magma supply to the crust is greater near segment centers resulting in a larger, more robust magma chamber and a shallower, more inflated ridge than near segment ends.

[1] Now at the Department of Terrestrial Magnetism, Carnegie Institution of Washington, Washington, D.C.

[2] Now at the Institute of Geophysics and Planetary Physics, Scripps Institution of Oceanography, La Jolla, California.

Paper number 97JB02349.
0148-0227/97/97JB-02349$09.00

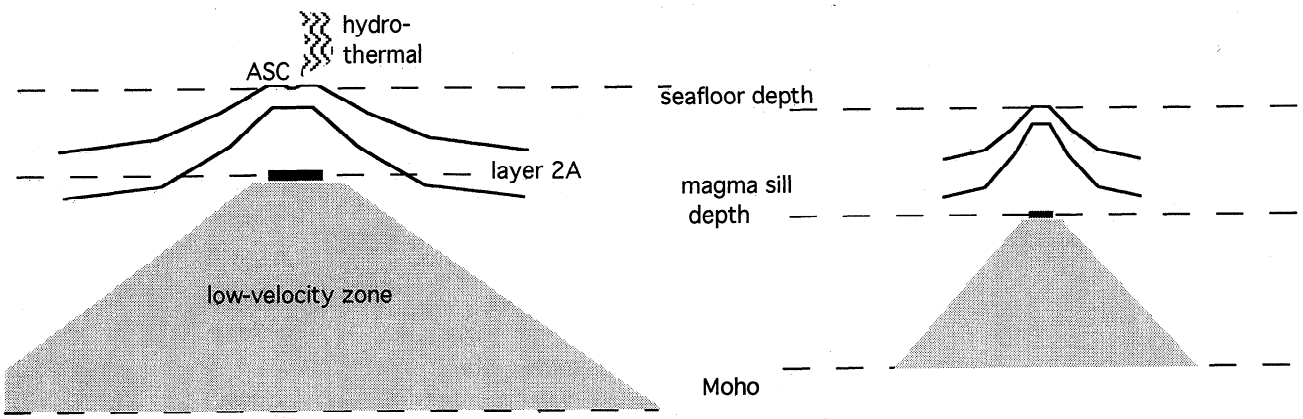

A. High Magma Budget

- thicker crust
- shallow water depth
- broad cross-sectional area
- wide low-velocity zone
  - high MgO content
  - high temperature
  - low density
- shallow melt lens
- thicker layer 2A
- ASC present
- hydrothermal venting

B. Low Magma Budget

- thinner crust
- deeper water depth
- narrow cross-sectional area
- narrow low-velocity zone
  - lower MgO content
  - lower temperature
  - higher density
- deeper melt lens
- thinner layer 2A
- no ASC present
- no hydrothermal venting

Figure 1. The current simple magma supply model describing the magmatic activity along the fast spreading East Pacific Rise predicts a contrast in ridge morphology and crustal structure between ridge sections with a high magma budget and those that have a low magma budget. ASC, axial summit caldera.

The relationship between magma supply and the morphological segmentation of the ridge is supported by the correlation between axial morphology and the presence or absence of the magma sill reflector, first noted by *Macdonald and Fox* [1988] for the 9-13°N EPR area. Seismic reflection data from the southern EPR are generally consistent with the association between shallow, inflated sections of the ridge and the presence of a midcrustal magma sill [*Scheirer and Macdonald*, 1993]. Locally, between 17°S and 17°30'S, *Mutter et al.* [1995] report that the magma sill becomes shallower and wider as the ridge axis becomes shallower and broader and use deviations from this expected relationship to suggest very recent or ongoing magmatic activity near 17°26'S. Seismic layer 2A in young oceanic crust is usually interpreted to be the volcanic extrusive section [e.g., *Christeson*, 1994; *Hooft et al.*, 1996]. It has been suggested that the thickness of the seismic layer 2A reflects the magma budget [*Harding et al.*, 1993]. Evidence for recent volcanism [*Haymon et al.*, 1993] and abundant hydrothermal activity [*Haymon et al.*, 1991] along the northern EPR near 9°50'N, as well as the general good correlation between morphological indicators of magma supply and the presence of hydrothermal plumes [*Baker*, 1996], are also consistent with the magma supply model summarized in Figure 1.

However, new results suggest that the relationship between morphological indicators of magma supply and axial crustal structure is more complicated than this simple model would predict. *Hussenoeder et al.* [1996a] have shown that the thickness and inferred crystal content of the magma lens along the northern and southern EPR are not correlated with axial depth. Variations in magma sill depth have been reported from both the northern [*Harding et al.*, 1993] and southern [*Detrick et al.*, 1993] EPR that are not related to changes in the depth or cross-sectional area of the ridge. *Lonsdale* [1983, 1986, 1989a, b] has questioned the correlation between segmentation of the magmatic system with that of the axial morphology and suggests that small overlapping spreading centers (OSCs) may be underlain by a single, wide crustal magma chamber. Seismic reflection data along the northern EPR and the Valu Fa ridge reveal wide magma sill reflectors beneath some OSCs [*Collier and Sinha*, 1990, 1992; *Kent et al.*, 1993a]. *Barth and Mutter* [1996] report that the crust is actually thinner beneath the inflated portion of the ridge at 9°50'N than elsewhere along this ridge segment. Similarly, despite large differences in the depth and morphology of the EPR on either side of the Clipperton transform, *Begnaud et al.* [1997] and *Posiolova et al.* [1995] find little difference in the thickness of crust on either side of the fracture zone.

Work at the intermediate spreading rate Valu Fa Ridge, a back arc spreading center in the Lau Basin, also reveals along-axis variations in ridge crest observables that are clearly incompatible with the simple magma supply model. A detailed seismic and gravity study shows that the magmatic system is segmented on a length scale of 10 km or less and that this magmatic segmentation does not correlate with the morphological segmentation of the ridge axis [*Collier and*

Sinha, 1990, 1992; *Sinha*, 1995]. In terms of axial morphology, the three ridge segments range from being shallow but narrow in the north to deep but wide in the south. This unusual inverse correlation between axial depth and width may be related to basalt compositions that range from andesitic basalt to rhyolite going from north to south [*Davis et al.*, 1991; *Fresnel et al.*, 1991]. Despite these morphological variations, there is a magma sill reflector which remains at an almost uniform depth of 3.2±0.2 km along all three ridge segments [*Collier and Sinha*, 1990, 1992]. There are, however, significant variations in the width and amplitude of the magma sill reflector which are correlated with the cross-sectional area of the ridge and are interpreted in terms of the temporal variability of the crustal accretion process [*Collier and Sinha*, 1992; *Weidicke and Collier*, 1993].

In this paper we examine the relationship among various indicators of magma supply along more than 800 km of the southern EPR. The variables we compare are axial depth, cross-sectional area of the ridge, layer 2A (extrusive layer) thickness on- and off-axis, the rate at which the extrusive layer thickens off-axis, magma sill depth and width, mantle Bouguer anomaly, temperature of the erupted lavas (MgO content), hydrothermal activity, and the presence of an axial summit caldera. We will show that the thickness of the extrusive section (seismic layer 2A), the properties of the magma sill (depth, width, thickness), and the intensity of hydrothermal venting are poorly correlated with morphological indicators of magma supply such as axial depth or ridge cross-sectional area. We explain these observations by proposing that the emplacement geometry (width of the dike intrusion zone and flow lengths), not magma supply, controls the extrusive (layer 2A) thickness. We also suggest that the melt lens properties and hydrothermal activity are closely linked to spreading events (dike intrusion, eruptions and faulting) which occur on much shorter time scales (~10-100 years) than the variations in magma supply and thermal state which are reflected in the ridge morphology (~100,000 years).

2. Seismic Data Processing and Analysis

In 1991 a multichannel seismic reflection survey imaged an ~800-km-long section of the southern East Pacific Rise (Figure 2) from the northern limb of the 20.7°S OSC to the Garrett fracture zone [*Detrick et al.*, 1993]. This extensive two-ship reflection/refraction survey concentrated on three areas centered at 14°15'S, 17°20'S, and over the 15°55'S OSC (Figure 2). Outside of these regions, reflection data were shot along the ridge axis and five additional across-axis seismic lines were obtained. The reflection data were acquired aboard R/V *Maurice Ewing* of the Lamont-Doherty Earth Observatory using a 4-km-long, 160-channel digital streamer with 25-m group separation. The source was a 20-gun, 8385-cubic-inch air gun array. For the lines north of 17°20'S, shots were fired every 20 s, yielding a shot spacing of 50 m and 40-fold coverage for a nominal ship speed of 5 knots. South of this area, port and starboard halves of the array were alternately fired every 10 s, yielding a shot spacing of 25 m and 80-fold coverage.

The multichannel seismic data were processed using SIOSEIS (written by P. Henkart, Scripps Institution of Oceanography, La Jolla, California). Shot gathers were sorted into 12.5-m bins producing common midpoint (CMP) gathers whose ranges extended between 263 and 4263 m. The along-axis data were stacked using a velocity model that varied with distance along the ridge crest. The normal moveout (NMO) velocities of the seafloor, layer 2A, and magma sill reflections were determined from constant velocity stacks of the data constructed at locations where preliminary stacks showed a change in crustal structure. Seafloor and postcritical reflections near the base of layer 2A were muted at ranges greater than 3200 m to prevent excessive stretching that occurs within the steep velocity gradient at the base of layer 2A. Muting of the farthest offsets (>3200 m) of the layer 2A reflection essentially includes only those rays which turn near the base of layer 2A thereby minimizing any errors associated with stacking these wide-angle reflections [*Harding et al.*, 1993]. The across-axis reflection profiles were stacked using a velocity model determined from constant velocity stacks made every 2.5 km. Exact-log dip moveout (DMO) corrections [*Liner*, 1990] were applied prior to stacking. Finally, the profiles were migrated using a finite difference time 45° algorithm [*Brysk*, 1983] to account for the two-dimensional velocity variations produced by seafloor and layer 2A topography. On the resulting profiles, the magma sill widths may be slightly overestimated due to energy diffracting off the edges of the sill [*Kent et al.*, 1990]; however, these errors are minimized by the finite difference migration.

The two-way travel time to the base of layer 2A and to the magma sill reflector were picked from the along- and across-axis seismic profiles at ~100 m spacing. The error for these picks is estimated to be ±0.003 s. There is a good agreement between picks of on-axis layer 2A thickness and magma sill depth made on across-axis profiles with those made at the intersection point on the along-axis profile. The excellent navigation of this experiment is confirmed by plots of the ship track superimposed on the multibeam bathymetry of the rise crest. Even in regions where the ship deviates from the center of the axial high, there is no consistent pattern of disappearance of the magma sill, or thickening of layer 2A. Two-way travel time picks were converted to depth using the composite velocity model of *Harding et al.* [1993] which includes a low-gradient layer (2.2 to 2.3 km/s) beneath the seafloor underlain by a layer with a high gradient (2.3 to 5.6 km/s). The ratio of the thicknesses of these two layers is held fixed (95:160 m), while their total thickness is varied to match the observed travel time. Using this conversion, the picking error results in a layer 2A thickness error of ±10 m.

The velocity structure used in this paper [*Harding et al.*, 1993] has a layer 2A which is faster, and concurrently thicker, than velocity-depth functions calculated recently from the same seismic data [*Carbotte et al.*, 1997; *Hussenoeder et al.*, 1996b; *Tolstoy et al.*, 1997]. However, the layer 2A thickness calculated using this slower velocity-depth profile is only reduced by ~20±3 m. In view of this small difference, we have continued using the velocity structure of *Harding et al.* [1993] since this maintains the comparability with measurements of layer 2A thickness made along the northern EPR. Considering the possible variability in shallow crustal velocity structure, we assign layer 2A thickness measurements an error of ±20 m.

The travel time between the base of layer 2A and the magma sill reflector was converted to thickness by assuming a linear gradient in velocity of 0.74 s^{-1} beneath the base of layer 2A. This leads to an error of ±25 m in depth to the magma sill reflector. On the across-axis multichannel seismic lines we

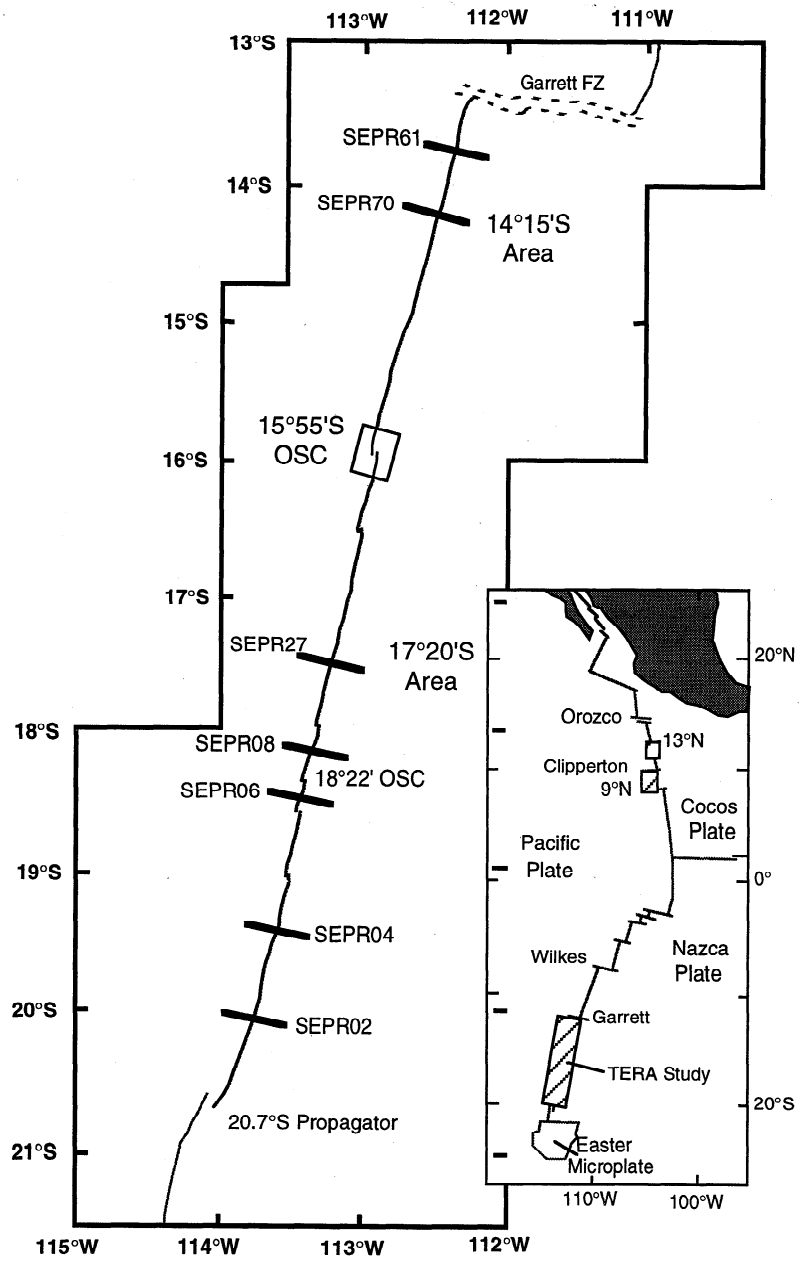

Figure 2. Map of the southern East Pacific Rise (SEPR). Major segment boundaries are indicated. A multichannel seismic line was shot along the ridge crest form the northern limb of the 20.7°S propagator to the Garrett fracture zone. Boxes indicate the intensive multichannel seismic study areas at 14°S, 15°55'S, and 17°S. The remaining five across-axis seismic lines are shown by dark lines, as well as the location of SEPR27 and SEPR70 in the intensive study areas at 17°S and 14°S, respectively.

measured the depth of the magma sill below the seafloor and its width, the on- and off-axis thickness of layer 2A and the rate at which the thickening occurs. Errors in the width of the magma sill reflector and in the rate of layer 2A thickening are estimated to be ±50 m and ±0.2 km, respectively; other errors are as quoted above. The axial depth, cross-sectional area [*Scheirer and Macdonald*, 1993], latitude, and measures of seismic structure for each of the across-axis lines are given in Table 1, in which we have also compiled the information from the across-axis seismic profiles shot in the intensive study area at 14°15'S [*Kent et al.*, 1994], and at 9°N on the northern EPR [*Harding et al.*, 1993; *Kent et al.*, 1993a, b]. All the seismic lines from the northern and southern EPR were processed and interpreted using exactly the same methods so intercomparison of the observations is possible. The variables obtained from the across-axis seismic data are spatially biased since the seismic lines for the SEPR were predominantly shot along closely spaced lines within three intensive study areas and coverage outside these regions is very poor. Therefore the across axis structural information is not representative of the range and distribution typical of the entire ridge crest. Correlation coefficients between axial depth, ridge cross-sectional area, and seismic crustal structure for the along- and across-axis lines are given in Table 2.

Table 1. Ridge Morphology, Magma Sill and Layer 2A Characteristics

Latitude	Line	Axial Depth, m	Cross-Sectional Area[a], km^2	Magma Sill		Layer 2A Thickness		
				Width, m	Depth, m	On-Axis, m	Off-Axis, m	Half Width, km
Error		±20	±0.5	±50	±25	±20	±20	±0.2
				Southern East Pacific Rise				
-20.16	SEPR02	2846	0.6		1060[b]	330	620	1.5
-19.44	SEPR04	2782	2.3	560	1110	240	410	0.7
-18.46	SEPR06	2619	4.9	300	1340	270	520	3.2
-18.21	SEPR08	2673	5.0	590	1550	200	350	1.2
-17.54	SEPR34	2611	5.2	740	1210	260	460	4.1
-17.46	SEPR26	2590	5.1	1540	1000	230	390	2.0
-17.44	SEPR33	2588	5.4	950	1190	247	530	2.3
-17.42	SEPR27	2591	5.6	850	760	230	570	3.0
-17.38	SEPR28	2611	5.5	710	1100	240	490	2.1
-17.33	SEPR32	2621	5.0	375	1350	210	530	1.3
-17.29	SEPR29	2621	5.4	875	1140	260	510	1.5
-17.24	SEPR31	2610	6.2	710	1110	250	530	1.3
-17.20	SEPR30	2605	5.8	560	1150	270	560	1.6
-17.16	SEPR11	2601	5.3	500	1210	260	450	1.9
-17.07	SEPR10	2628	5.4	1010	1260	240	480	2.2
-14.49	SEPR57	2631	4.3	650[c]	1100[d]	240[d]	570[c]	1.8[c]
-14.45	SEPR68	2628	4.2	400[c]	1000[d]	270[d]	540[c]	1.5[c]
-14.41	SEPR56	2630	4.4	700[c]	990[d]	190[d]	540[c]	2.3[c]
-14.37	SEPR67	2634	4.5	1050[c]	940[d]	270[d]	540[c]	2.7[c]
-14.33	SEPR69	2636	4.9	950[c]	960[d]	280[d]	570[c]	2.5[c]
-14.29	SEPR66	2640	5.0	750[c]	1040[d]	210[d]	530[c]	2.8[c]
-14.25	SEPR70	2642	4.8	750[c]	1080[d]	220[d]	510[c]	3.4[c]
-14.21	SEPR65	2638	4.4	700[c]	1100[d]	240[d]	530[c]	3.2[c]
-14.17	SEPR71	2635	4.6	750[c]	1220[d]	270[d]	540[c]	3.4[c]
-14.13	SEPR64	2636	4.2	375[c]	1250[d]	240[d]	510[c]	2.9[c]
-14.09	SEPR72	2635	4.7	550[c]	1120[d]	250[d]	540[c]	2.4[c]
-14.05	SEPR63	2634	4.8	550[c]	1220[d]	210[d]	530[c]	2.8[c]
-14.01	SEPR46	2636	4.9	400[c]	1220[d]	270[d]	550[c]	2.7[c]
-13.81	SEPR61	2640	4.5	690	1200	200	520	1.9
Mean		2640	4.7	680	1140	245	515	2.3
s.d.		50	1.1	260	150	30	57	0.8
				Northern East Pacific Rise				
+08.92	CDP37	2580	3.5	750[e]	1660[e]	380[f]	560[g]	2.1[g]
+09.31	CDP33	2590	3.2	4100[h]	1500[h]	200[f]	510[g]	1.6[g]
+09.49	CDP31	2580	3.6	1200[h]	1560[h]	180[f]	450[g]	4.1[g]
+09.66	CDP29	2560	3.6	700[h]	1550[h]	230[f]	440[g]	2.3[g]
+09.83	CDP27	2510	4.0	500[h]	1430[h]	280[f]	460[g]	2.5[g]
Mean		2570	3.6	788[i]	1540	254	484	2.5
s.d.		40	0.3	295[i]	85	80	50	0.9

[a] Interpolated from *Scheirer and Macdonald* [1993].
[b] From the along axis data.
[c] *Kent et al.* [1994].
[d] Picked by EEEH and calculated using *Kent et al.* [1994].
[e] *Kent et al.* [1993a].
[f] Picked by EEEH and calculated using *Harding et al.* [1993].
[g] *Harding et al.* [1993].
[h] *Kent et al.* [1993b].
[i] Calculated by excluding CDP 33. Including CDP33: 1450±1500.

3. Results

3.1. Variation in Seismic Structure Along the SEPR

The SEPR has a relatively uniform depth from the Garrett transform to about 18.5°S and then deepens systematically towards the large overlapping spreading center (OSC) at 20.7°S (Figure 3a). The regional variation in crustal structure along this portion of the SEPR can be divided into northern, central, and southern ridge sections bounded by the Garrett transform, the 15°55'S and 17°55'S OSCs, and the large 20.7°S OSC, respectively. These sections of ridge are based on differences in the range and variability of the observed crustal structure as determined from the variation in seafloor depth, extrusive layer thickness and magma sill depth. *Sinton et al.* [1991] define two primary magmatic segments delimited by

Table 2. Correlation Coefficients for Across-Axis and Along-Axis Data From the Southern EPR

	Water Depth	Cross-Sectional Area[a]	Magma Sill Width	Magma Sill Depth	Layer 2A Thickness On-Axis	Layer 2A Thickness Off-Axis	Layer 2A Thickness Half Width
Correlation Coefficients for the Across-Axis Data, N=29							
Axial depth	1.00	0.93	0.21	0.11	-0.36	-0.18	0.23
Cross-Sectional Area[a]	0.93	1.00	0.26	-0.03	-0.33	-0.06	0.35
Magma Sill							
Width	0.21	0.26	1.00	-0.45	-0.03	-0.20	0.08
Depth	0.11	-0.03	-0.45	1.00	-0.17	-0.44	-0.12
Layer 2A							
On-Axis	-0.36	-0.33	-0.03	-0.17	1.00	0.40	0.02
Off-Axis	-0.18	-0.06	-0.20	-0.44	0.40	1.00	0.20
Half Width	0.23	0.35	0.08	-0.12	0.02	0.20	1.00
Correlation Coefficients for the Along-Axis Data, N>4071							
Axial depth	1.00	0.79		-0.05	-0.96		
Cross-Sectional Area[a]	0.79	1.00		0.11	-0.70		
Magma Sill							
Width							
Depth	-0.05	0.11		1.00	0.34		
Layer 2A							
On-Axis	-0.96	-0.70		0.34	1.00		
Off-Axis							
Half Width							

[a] Interpolated from *Scheirer and Macdonald* [1993].

the Garrett transform to 15°55'S and by 15°55'S-20°40'S, each of which has a distinct mantle source composition. The secondary magmatic segments defined by *Sinton et al.* [1991] (Figure 3c) are subsections within three structurally defined ridge sections; the southern section consists of magmatic segments G, H, I, and J; the central section consists of magmatic segments L and K; and the northern section consists of magmatic segments M, N, and O. Along the northern section of ridge the axis is broad, shallow, and remarkably uniform in depth. The axis remains shallow and is very broad along the central section but shows a slightly greater along-axis variability in seafloor depth. Between 17°S and 18°S the ridge has the most inflated morphology of the entire SEPR region. Along the southern section the ridge deepens and narrows rapidly from a shallow point in the "Hump" region at 18°27'S to the large 20.7°S OSC. The along-axis variability in axial depth increases from north to south. The intensive seismic studies were located at the 15°55'S OSC and at latitudes 14°15'S and 17°20'S, where the ridge is broad and shallow and has the morphological characteristics of a high magma budget.

Figure 4 shows four examples of across- and along-axis multichannel profiles from the SEPR. These seismic profiles illustrate the crustal structure of parts of the ridge ranging from inflated to magma-starved in morphology. Figure 4a is from the 17°20'S intensive study area, a portion of the ridge along the central segment with an extremely inflated morphology (cross-sectional area of 5.6 km^2). Figure 4a (top) shows an across-axis profile at 17°26'S (SEPR27) and illustrates the general features of the crustal structure of a fast-spreading ridge. The seafloor is shallowest at the axis and deepens on either side of the ridge. In cross-section the ridge has a broad, domed shape. Wide-angle reflections from the base of layer 2A are imaged ~0.15 s below the seafloor at the ridge axis. Seismic layer 2A, which we correlate with the volcanic extrusive layer [*Herron*, 1982; *Harding et al.*, 1989; *Christeson et al.*, 1992], is 230 m thick at the ridge axis and doubles in thickness (570 m) within 3 km on either side of the ridge. The magma sill lies at 3.85 s, a depth of 760 m below the seafloor, and has a width of 850 m.

As the ridge deepens and narrows, the ridge morphology and crustal structure change. Figures 4b and 4c are from the northern and southern segments (latitudes 14°15' S, SEPR70, and 18°28'S, SEPR06), respectively, regions with a morphology indicative of a medium magma supply (cross-sectional areas of 4.8 and 4.9 km^2, respectively). The quality of the data on lines SEPR01 through SEPR10 is not as high as for the other seismic lines because a 10-s shooting rate, though increasing the fold of the data, introduces noise due to reverberation of the previous shot in the water column. The ridge in these regions has a domed but narrower axial high, and the axial depths are slightly greater than in Figure 4a. The on-axis thickness of layer 2A on SEPR70 (220 m) is about the same as in Figure 4a, while on SEPR06 it is somewhat greater (270 m). The off-axis thicknesses of layer 2A (510 and 520 m, respectively) are again about twice the on-axis values. The rate of layer 2A thickening on these two profiles is somewhat less than in the previous case, with half widths of thickening of 3.4 and 3.2 km, respectively. The magma sill on SEPR70 is relatively shallow (1080 m below the seafloor) and wide (750 m), while on SEPR06 it is deeper (1340 m), narrower (~300 m), and associated with a weaker reflection. The weak reflection on the across-axis profile may be due to the scattering of energy from seafloor topography. On the along-axis line, where topographic effects are less of a problem, the magma sill reflector is high amplitude.

Figure 4d is from where the southern segment deepens toward the 20.7°S OSC, a region with an extremely magma-starved morphology (cross-sectional area of 0.6 km^2, latitude 20°10'S). The ridge is significantly deeper (2846 m) and very

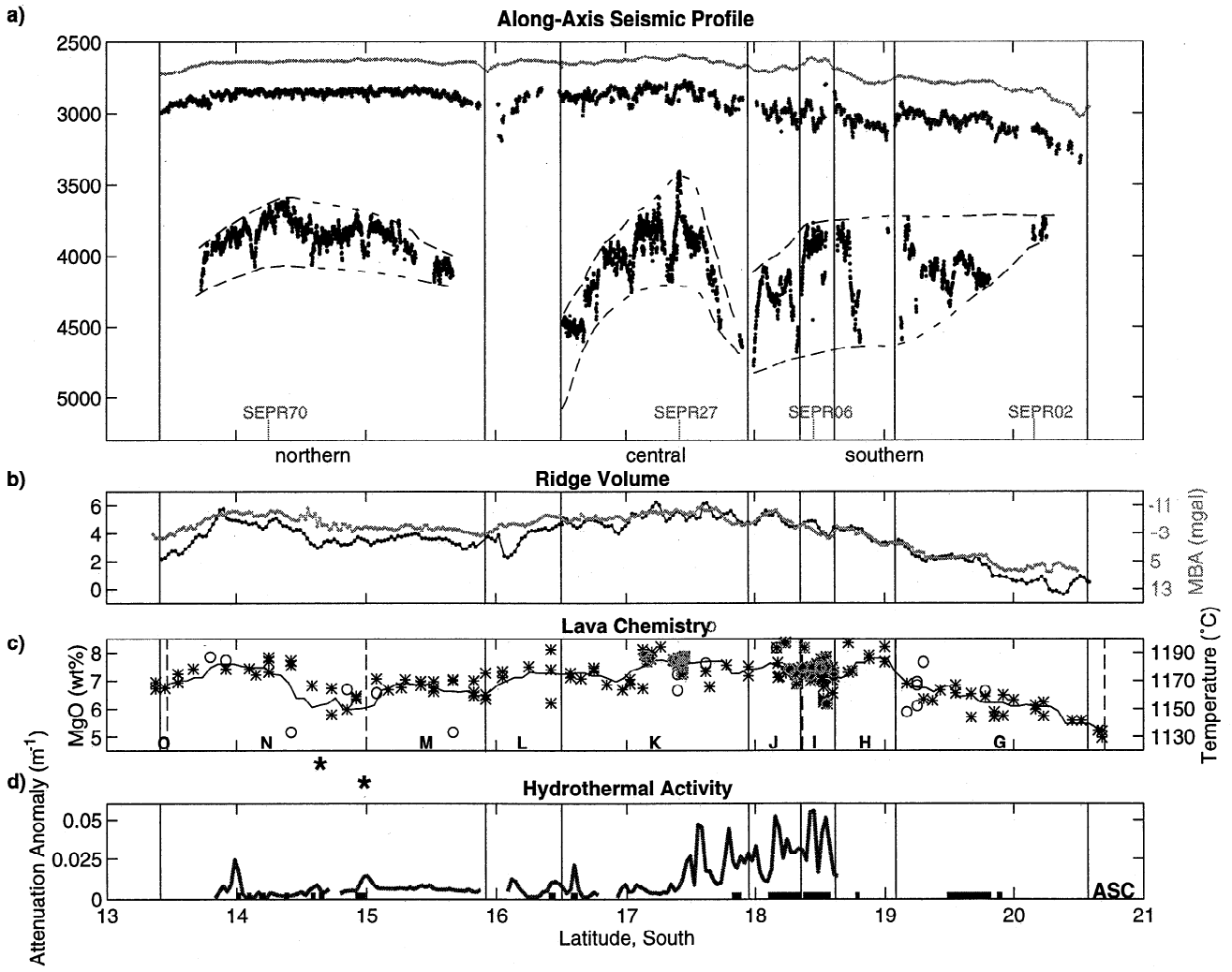

Figure 3. Along-axis summary of the seismic structure and other indicators of magma budget along the ridge crest of the SEPR from the northern limb of the 20.7°S propagator to the Garrett fracture zone (13.4°S), >800 km. Overlapping spreading centers (OSCs) are indicated by vertical lines. The northern, central and southern ridge sections of the SEPR are defined based on differences in the range and variability of the observed crustal structure as determined from the seafloor depth, extrusive thickness, and magma sill depth and are bounded by the Garrett transform, the 15°55'S and 17°55'S OSCs, and the large 20.7°S OSC. (a) Seafloor topography (light grey) [*Tighe et al.*, 1988], depth to the base of the extrusive layer (layer 2A) (dark grey), and the magma sill reflector (black). The error for seafloor and layer 2A depth is ±20 m, while that for the magma sill depth is ±25 m. Note the relatively uniform thickness of layer 2A and the large variability in magma sill depth. The general trend of magma sill depth along the northern, central, and southern ridge sections is outlined (dashed line). Locations of the across-axis seismic profiles shown in Figure 4 are indicated in light grey. (b) Cross-sectional area of the ridge (dark) [*Scheirer and Macdonald*, 1993] (error is ±0.5 km^2) and the mantle Bouguer anomaly (light grey) [*Magde et al.*, 1995] (error is ±1 mGal). Note the excellent correlation between these two measures of the volume of the crustal low-velocity zone. (c) MgO weight percent for basalt samples (standard deviation of measurement typically 0.11) dredged from the ridge axis (asterisks) [*Sinton et al.*, 1991]. T-MORBs are indicated by black open circles. Samples collected from the youngest on-axis flows during *Nautile* submersible dives (grey open circles) [pers. comm., Sinton, 1995] and do not deviate much from the dredge samples collected in the same area. There is a variability of ~±1 weight percent in these data. The curve represents a running mean made through the data to show the local trend. The scale on the right-hand side shows the corresponding lava temperatures (error ~3°C) calcuated using the olivine thermometer of *Sisson and Grove* [1993]. The letters at the bottom are the nomenclature used for the different magmatic segments defined by *Sinton et al.* [1991]. (d) Light attenuation (resolution is 0.001 m^{-1}) in the water column integrated from 100 to 300 m above the seafloor in bins of 0.03° [*Baker and Urabe*, 1996]. Note the large variability in the location of hydrothermal fields. Along the x axis the dark bars show the portions of the ridge along which *Lonsdale* [1989b] located an ASC or axial graben using Sea Beam data. There is a better correlation between hydrothermal venting and the presence of an ASC than with the presence or depth variations of the magma sill.

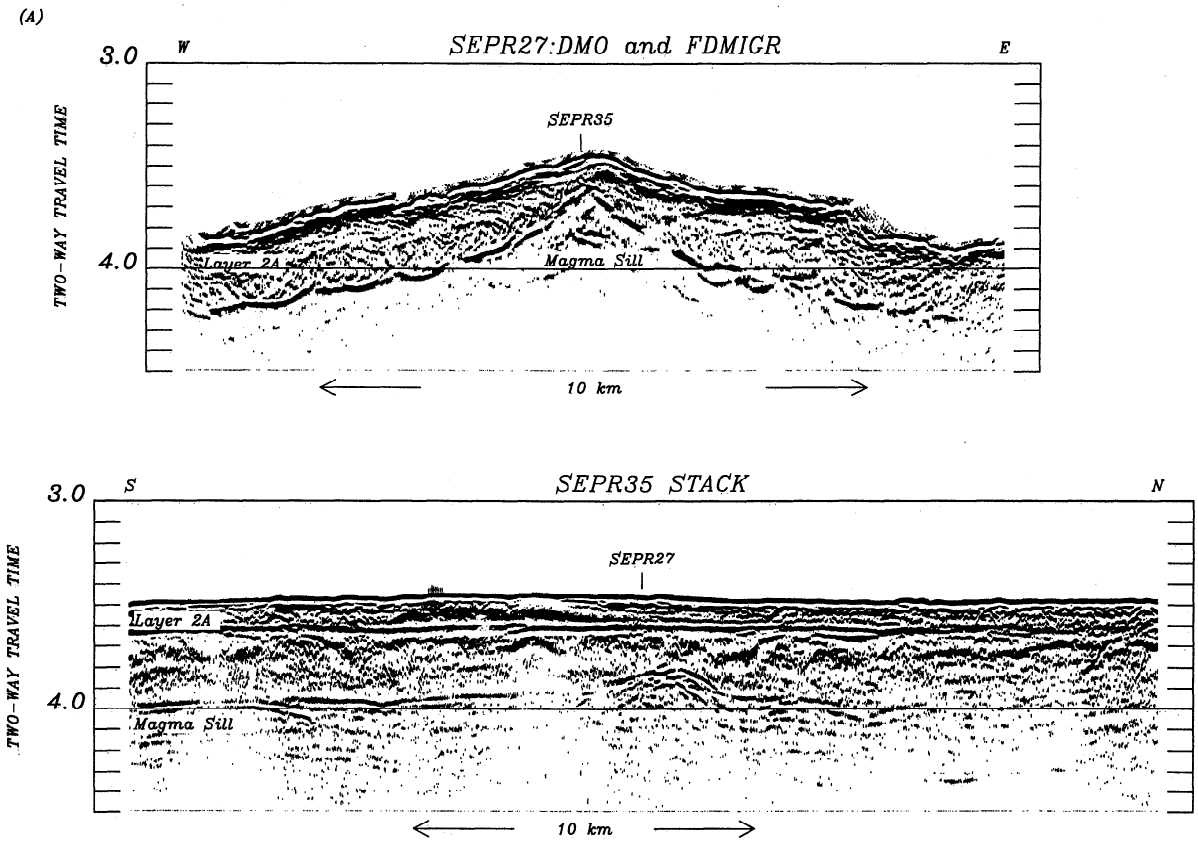

Figure 4. Along- and across-axis seismic lines from four areas of the ridge that range from inflated to magma starved. The across-axis data have had prestack DMO applied, then were stacked and finite difference migrated to correct for seafloor and layer 2A topography. Note the range in widths of the ridge crest, the amount of topography, and the differences in the thickening profiles of layer 2A. The along-axis lines show the stacked multichannel seismic section. The depth and nature of the layer 2A reflection are very uniform everywhere along the axis. In contrast, there are significant along-axis differences in the depth of the magma sill reflector. (a) Across-axis profile SEPR27 at 17°25'S and along-axis profile SEPR35 from 17°32'S to 17°15'S. The ridge is shallow and has a wide domed morphology. At 17°24'N, just north of the shallowest and broadest portion of the ridge, the melt lens shoals from an average depth of 1150 m to 800 m below the seafloor over a distance of 4 km. (b) Across-axis profile SEPR70 at 14°15'S and along-axis profile SEPR45 from 14°23'S to 14°07'S. The magma sill is shallow and relatively uniform in depth (1080 m below the seafloor). Note the graben on west side of the ridge on the across-axis profile. (c) Across-axis profile SEPR06 at 18°28'S and along-axis profiles SEPR05 and SEPR07 from 18°37'S to 18°21'S. The axial summit graben can be seen on the across-axis profile. The magma sill lies at a deeper depth (1340 m below the seafloor) and deepens toward the OSCs at 18°39'S and 18°21'S. Note that SEPR70 and SEPR06 have similar cross-sectional areas and yet there is a large difference in magma sill depth between the two. (d) Across-axis profile SEPR02 at 20°10'S and along-axis profiles SEPR01 and SEPR03 from 20°17'S to 20°01'S. The ridge is deep and very narrow in this region, and there is evidence for significant tectonism on the flanks. From 20°10' to 15'S on the along-axis line a small, and surprisingly shallow (1060 m below the seafloor), magma lens is imaged despite the magma-starved morphology.

narrow and triangular in shape. On this profile (SEPR02) the seafloor is fairly rough which leads to more scattering. The 10-s shooting rate on this profile also reduces the quality of the image of the crustal structure. The along-axis data reveal a magma sill at this location, but it is so weak that on the across-axis profile it can only be seen in constant velocity stacks. This magma sill has an unusually shallow depth given the morphology. On-axis layer 2A is thicker on this profile (330 m) and thickens more rapidly (half width of thickening of 1.5 km) than on other profiles to attain an off-axis thickness of 620 m.

The three sections of ridge described above show significant differences in the range and variability of the seismic crustal structure. While the extrusive layer (seismic layer 2A) has a comparatively uniform thickness over the entire region (median on-axis thickness is 235 m; range 200-300 m; see Figure 5), there are differences in the thickness and variability of layer 2A between the three ridge sections. The northern section has a very uniform 2A thickness (222±21 m), the central section shows more variability in thickness (233±48 m), and the southern section of ridge has the thickest and most variable extrusive layer (284±56 m). It appears that some thickening of layer 2A occurs toward ridge axis discontinuities (shown as vertical lines on Figure 3). This is particularly clear near the 15°55'S OSC.

In contrast to the small changes in extrusive layer

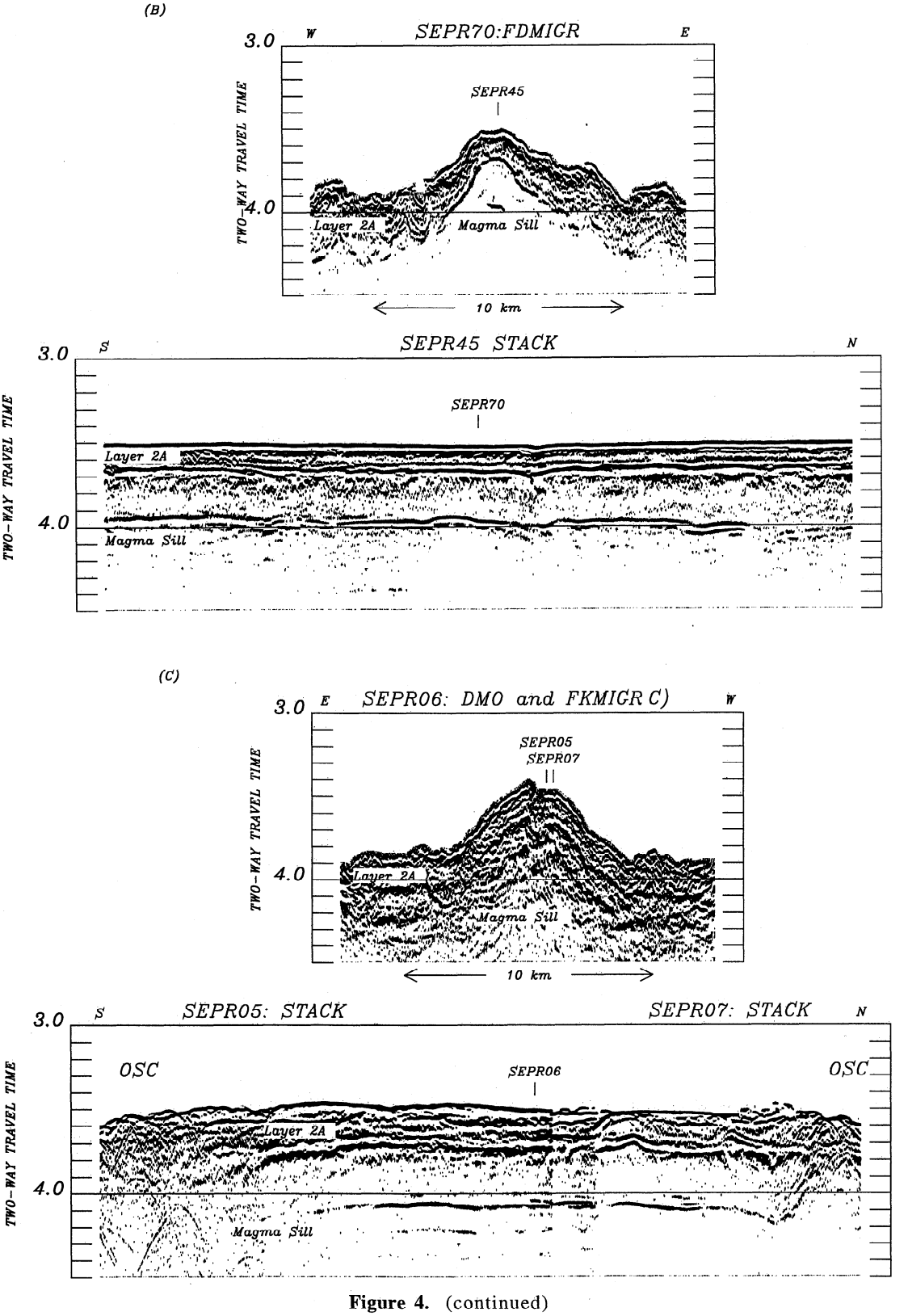

Figure 4. (continued)

thickness along-axis, the depth of the magma sill is quite variable along the study area (Figure 3a). It ranges in depth from 800 to 2000 m below the seafloor with a median depth of 1300 m (Figure 5). The northern and central ridge sections exhibit a general along-axis doming of the magma sill (shown by a dashed line in Figure 3a). On average, the magma sill is deeper near the ends of the ridge sections and shallower near the midpoint. However, there are also local changes in magma sill depth (~500 m over a distance of ~20 km) superimposed on these general trends. Along the northern ridge section the depth to the magma sill is relatively uniform (1220±110 m). The local variability in magma sill depth is small and mirrors

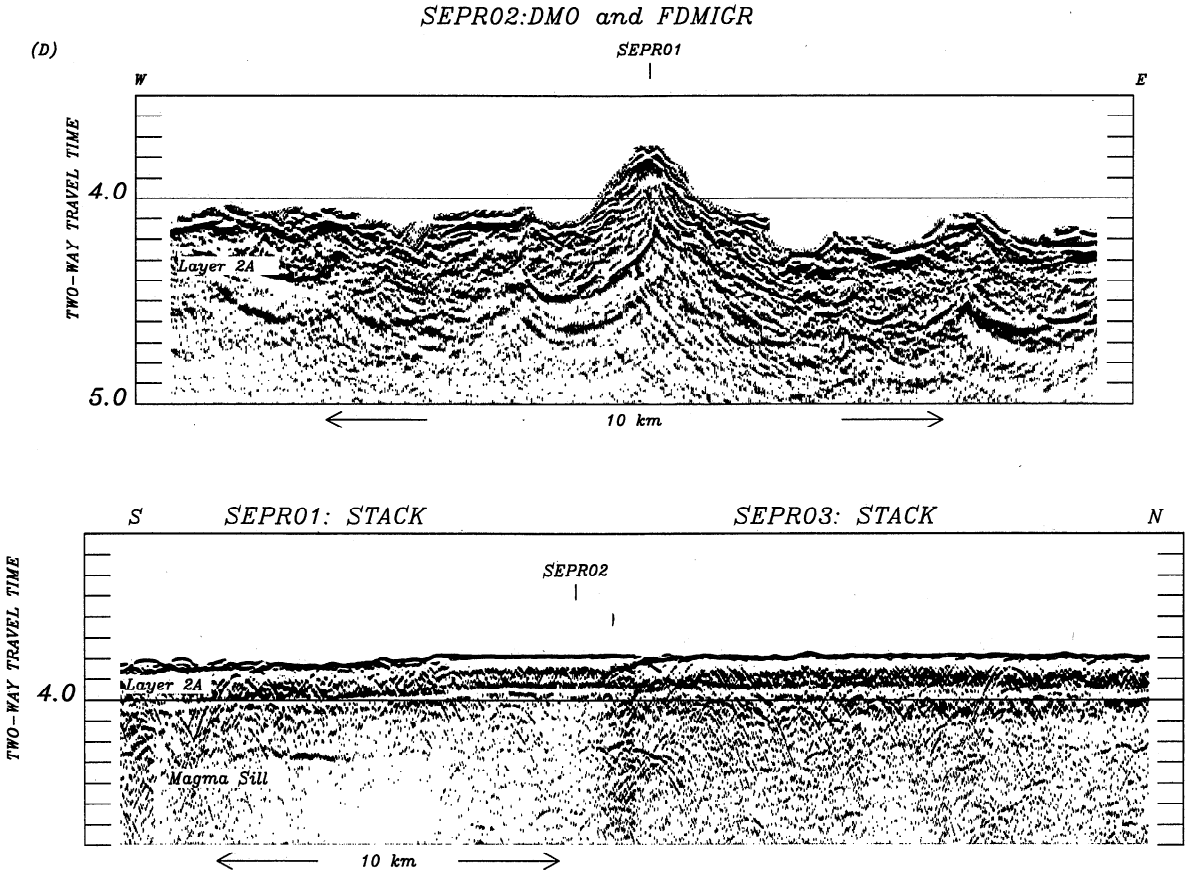

Figure 4. (continued)

the relatively uniform axial depths. Along the central section of ridge, the magma sill is on average somewhat deeper and shows a much greater depth range (820 to 2000 m with a median depth of 1350 m). The shallowest lens is observed at 17°25'S, where the magma sill shoals from 1350 m below the seafloor to 820 m over a distance of only 4 km (Figure 4a).

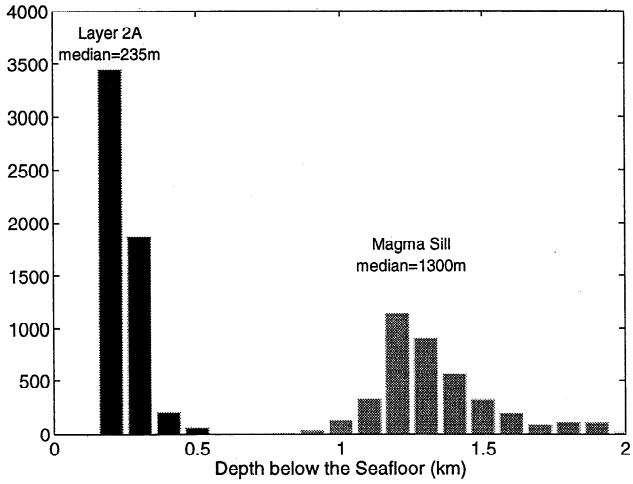

Figure 5. Histograms of layer 2A and magma sill depth from the SEPR. Data are binned at 100 m, and the median layer 2A thickness and magma sill depths are indicated. This emphasizes the uniformity of layer 2A thickness on the ridge crest and the much larger variability of magma sill depth.

Doming of the magma sill on a wavelength of 10 to 20 km (e.g., between 17° and 17°20'S) may be associated with individual volcanic constructs (personal communication J. M. Sinton, 1995). Along the southern section of the study area the magma sill is observed more sporadically. The depth range is similar to that of the central section (1350±210 m), but changes in magma sill depth are very abrupt and show no consistent pattern. Despite the magma-starved ridge morphology, an unusually shallow magma sill (896 m) is imaged at 20°15'S (Figure 4d).

3.2. Correlations With Indicators of Magma Supply

We compare the variations in seismic crustal structure along the SEPR described above with various indicators of magma supply (Figure 3). The ridge crest observables used are: the depth of the seafloor at a 1-km spacing obtained from the University of Rhode Island Sea Beam data synthesis [*Tighe et al.*, 1988] (resolution 10-20 m); cross-sectional area measured at 1 km intervals along the ridge from *Scheirer and Macdonald* [1993] (resolution ±0.5 km^2); the along-axis mantle Bouguer anomaly calculated at 2 km intervals from *Magde et al.* [1995] (error ±1 mGal); MgO weight percent of lavas dredged from the ridge axis from *Sinton et al.* [1991] and samples collected from the youngest on-axis flows by the submersible *Nautile* [*Auzende et al.*, 1996] (average standard deviation of analysis is 0.11); light attenuation in the water column integrated from 100 to 300 m above the seafloor in bins of 1.8 min (≈ 3 km) from *Baker and Urabe* [1996] (resolution ±0.001 m^{-1}); and the

locations along the ridge where *Lonsdale* [1989b] detected an ASC or an axial summit graben using Sea Beam data.

3.2.1 Morphology and gravity. Axial depth, ridge cross-sectional area, and along-axis mantle Bouguer anomaly are all well correlated (Figure 6). The ridge axis becomes deeper as the cross-sectional area of the ridge decreases and at the same time the mantle Bouguer anomaly increases, indicating higher subsurface densities. The along-axis variation in gravity (range of 20 mGal) and part of the axial depth changes (range of 400 m) can be explained by a decrease in crustal thickness of ~500 m between 18°S and 20°S [*Cormier and Macdonald*, 1995]. The ridge topography is supported by a low-density volume underlying the ridge crest, which is partitioned between the crust and the mantle [*Wilson*, 1992; *Wang and Cochran*, 1993; *Magde et al.*, 1995; R. Buck, Narrow flexural response to a broad load: Implications for axial highs and mantle dynamics at fast spreading mid-ocean ridges, submitted to *Journal of Geophysical Research*, 1997, hereafter referred to as Buck, submitted manuscript]. The variation in cross-sectional area (range of 6 km^2) suggests a change in volume of the hot, low-density region in the lower crust accompanied by a variation in the density anomaly in a narrow, deep region in the mantle [*Magde et al.*, 1995]. An alternative explanation calls on a broader region of upwelling in the mantle and attributes changes in cross-sectional area of the axial high to differences in lithospheric thickness along the axis (Buck, submitted manuscript, 1997). Thus along-axis variations in axial depth and ridge cross-sectional area are indicative of variations in magma supply to the ridge. Based on the time required to construct the axial high area, along-axis variations in magma supply are probably maintained of order of 100,000 years [*Scheirer and Macdonald*, 1993]. At 9°N on the EPR, off-axis seismic crustal thickness also indicates that the average rate of magma supply changes little over several hundred thousand years [*Barth and Mutter*, 1996].

Seismic crustal thickness is one of the most direct measures of ridge crest magma supply, provided that there is no strong along-axis transport of melt at crustal levels. Unfortunately, for this study, no measurements of seismic crustal thickness could be obtained on the along-axis seismic line due to shadowing by the lower crustal low-velocity zone. Moho can be observed on refraction data in the three survey areas centered at 14°15'S and 17°20'S, and over the 15°55'S OSC [*Detrick et al.*, 1993]. In the 14°15'S study area the Moho has been clearly imaged on across-axis multichannel reflection profiles [*Kent et al.*, 1994]. However, the Moho is not well imaged on a broader scale, and no direct measure of the regional variations in seismic crustal thickness can be made.

3.2.2. Basalt geochemistry. The variation in basalt geochemistry along the SEPR is shown in Figure 7 [*Sinton et al.*, 1991]. The geochemical variation in NaO and FeO corrected for low-pressure fractionation ($Na_{8.0}$ and $Fe_{8.0}$ calculated using the regression of *Sinton et al.* [1991] (Table 2)) indicate the extent and depth of melting within the mantle. The variability in $Na_{8.0}$ and $Fe_{8.0}$ is low (Figures 7d and 7e) and does not show any systematic pattern in the extent or depth of melting along the SEPR. This is consistent with the small along-axis variations in crustal thickness inferred from gravity data in this area [*Cormier and Macdonald*, 1995; *Magde et al.*, 1995]. Diapiric feeding of fast spreading ridge axes has recently been suggested by *Nicolas et al.* [1996] and *Wang et al.* [1996]. This melt supply model would predict higher $Fe_{8.0}$ and lower $Na_{8.0}$ near segment midpoints due to a greater depth and extent of melting although significant along-axis crustal level transport of melt would smooth out these initial variations. For this data set, $Fe_{8.0}$ and $Na_{8.0}$ show a weak negative correlation (correlation coefficient R^2 =

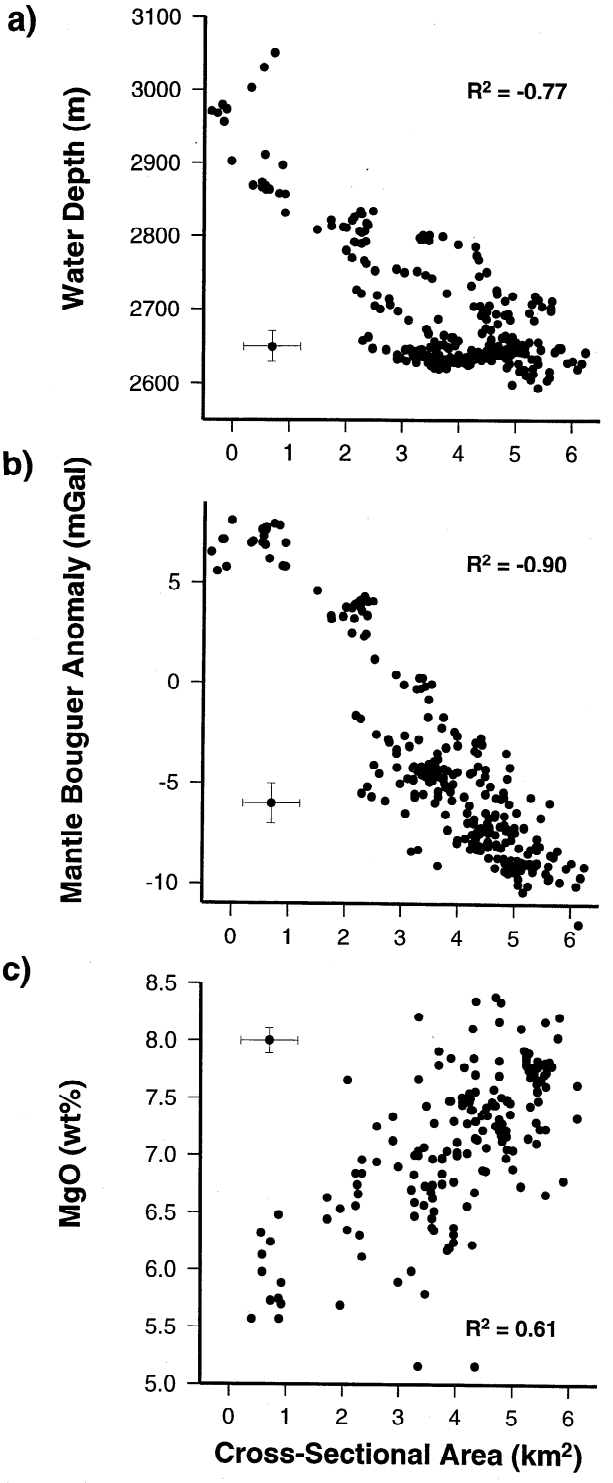

Figure 6. Plots showing (a) water depth, (b) mantle Bouguer anomaly, and (c) MgO content of dredged lavas for the SEPR plotted as a function of cross-sectional area. Correlation coefficients for these variables, R^2, and a generalized error bar are shown.

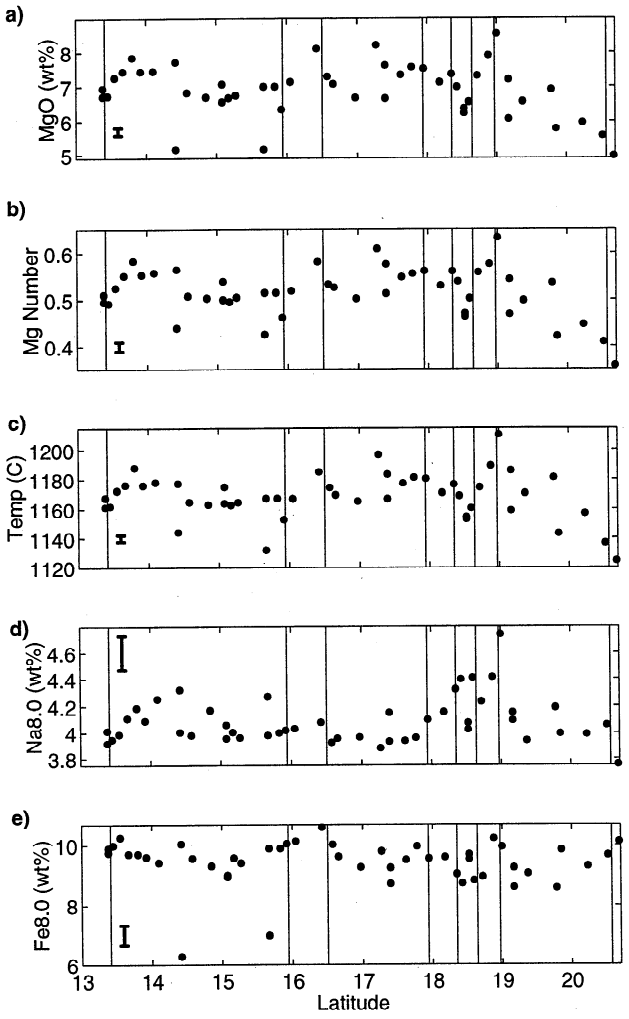

Figure 7. Major element geochemistry of lavas dredged from the ridge axis (representative glass analyses from *Sinton et al.* [1991 Table 1]. OSCs are shown by solid lines as in Figure 3. (a) MgO content in weight percent. (b) Mg number = (Mg/Mg+Fe molar). (c) Lava temperature calculated from the major element composition using the olivine thermometer of *Sisson and Grove* [1993] assuming atmospheric pressure and no water content. (d) $Na_{8.0}$ and (e) $Fe_{8.0}$ calculated using the regression of *Sinton et al.* [1991] (Table 2). Error bars are shown on the left-hand side.

-0.57). However, variations in $Na_{8.0}$ and $Fe_{8.0}$ do not correlate with variations in ridge cross-sectional area, Mg number, mantle Bouguer anomaly, nor magma sill depth. For example, the higher $Na_{8.0}$ values observed along the inflated ridge section between 14°S and 15°S are opposite of what would be expected if a mantle diapir with greater extent of melting were located beneath this section of ridge. The manner in which melt is supplied to the ridge from the mantle appears to be complicated. However, the correlation of mantle Bouguer anomaly variations with cross-sectional area and axial depth does suggest that there are broad scale variations in the melt supply to the SEPR on timescales of ~100,000 years.

The MgO content (and thus the temperature) of the erupted lavas correlates well with cross-sectional area (Figures 6c, 3b and 3c). The MgO content of basalts reflects the amount of fractional crystallization that the lavas have undergone in the crust. If the parental compositions are similar, MgO content is related to eruption temperature. For the lavas from the SEPR, MgO contents range from 5 to 8.5 weight percent (σ=0.11) with a corresponding change in Mg number from 0.35 to 0.64 (±0.01) (Figures 7a and 7b). Applying the olivine thermometer of *Sisson and Grove* [1993] to representative along-axis major element compositions [*Sinton et al.*, 1991], we obtain an approximately linear relationship between MgO content, Mg number, and lava temperature for this area (Figures 7a-7c). Eruption temperatures range from 1100°C to 1210°C (±3°C). The correlation between MgO and cross-sectional area, or alternatively the width of the axial high, which has also been noted previously [*Langmuir et al.*, 1986; *Scheirer and Macdonald*, 1993], suggests that along morphologically inflated sections of the ridge the erupted lavas are more primitive and reside in the crust for a shorter time.

3.2.3. Magma sill properties. *Purdy et al.* [1992] have proposed that on average, magma sill reflector depth decreases with increasing spreading rate beneath fast and intermediate spreading centers. The average depth of the magma sill is indeed greater on the northern EPR than on the southern EPR (Table 1). Spreading rate along the SEPR varies from a full rate of 137 mm/yr at 13.8°S to 144 mm/yr at 20°S for 0 to 0.73 Myr, while along the northern EPR, spreading rates are slower, ~105 mm/yr [*DeMets et al.*, 1994]. The difference in mean magma sill depth between the northern and southern EPR is 400 m (1140±150 m to 1540±85 m below the seafloor, respectively), which is greater than the standard deviation of the averages. On the other hand, there is no significant difference in the average width of the magma sill between the northern and southern EPR (680±280 m and 788±295 m, respectively, Table 1.) The regionally averaged depth but not width of the magma sill appears to depend on spreading rate.

Along the SEPR, where spreading rates vary by less than 10 mm/yr, the magma sill properties (depth and width) are quite variable and not well-correlated with axial depth, cross-sectional area, or MgO weight percent of erupted lavas (Figure 8). The magma sill shows a large range of depths along the SEPR from 800 to 2000 m (Figure 5), especially in comparison to the relatively uniform axial depth. A plot of magma sill depth versus cross-sectional area (Figure 8b) also shows a large amount of scatter. Similarly, lava eruption temperature (MgO content) does not correlate with magma sill depth (Figure 8c). In spite of the poor spatial coverage of the across axis lines, we find that magma sill widths are also quite variable and do not correlate with either axial depth or cross-sectional area (Figures 8d and 8e). The across-axis lines also show that on the regional scale, there is a great range in magma sill width for any given magma sill depth (Figure 8f). Thus the width and depth of the magma sill are extremely variable along the SEPR and show little relationship with morphological indicators of magma supply.

The observation that EPR lavas are not geochemically homogenized has been interpreted to mean that a continuous magma chamber can exist only if there are many separate regions of supply from below the crust and the magma chamber is not well mixed [*Langmuir et al.*, 1986]. This supports the rapidly varying nature of the magma sill that we have noted. A magma sill which is not completely molten [*Hussenoeder et al.*, 1996a] would probably be less well

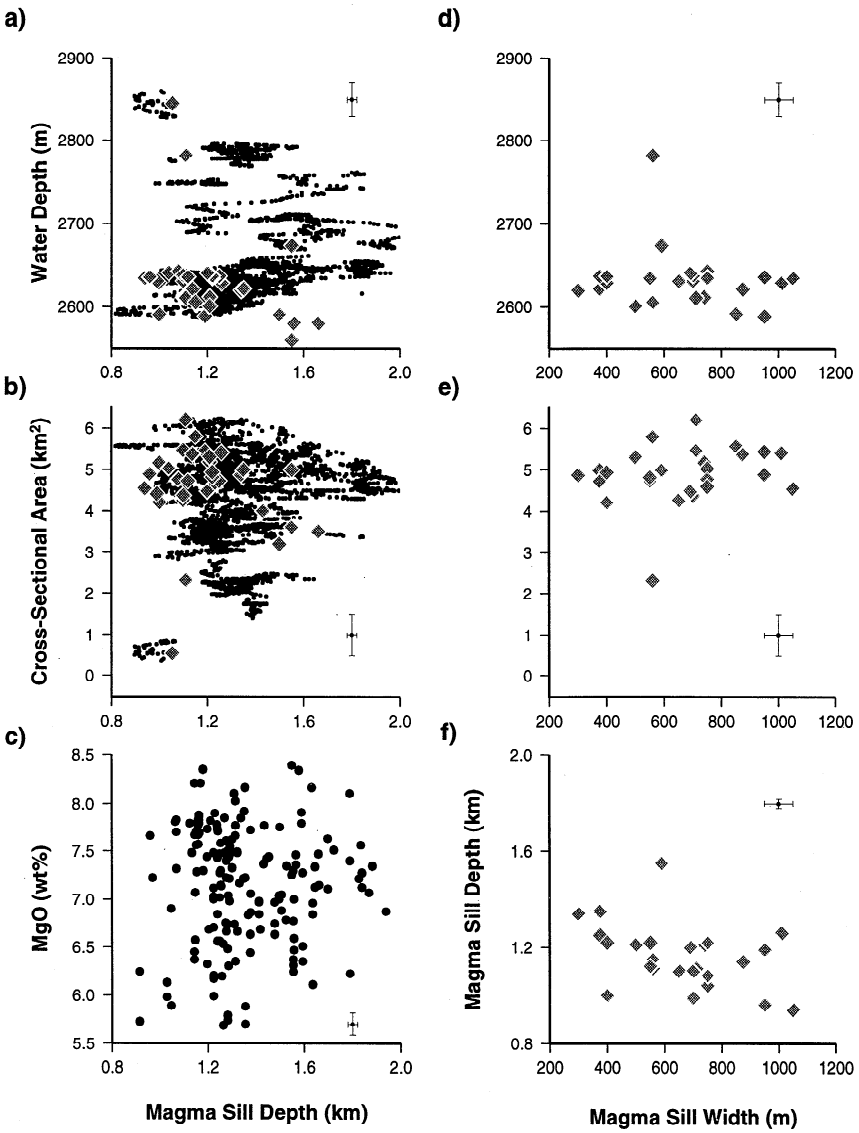

Figure 8. Relationships between indicators of magma budget and magma sill characteristics. (a) Water depth, (b) cross-sectional area, and (c) MgO weight percent plotted as a function of magma sill depth and (d-f) as a function of magma sill width. All the along-axis data points are shown as dots, the measurements based on the across-axis lines are shown as grey diamonds, and a generalized error bar is also shown. The correlation coefficients for these relationships are given in Table 2. Note the large variability in magma sill depth which does not correlate with indicators of magma budget.

mixed. The magmatic system at fast spreading ridges is complicated, consisting of a mostly molten magma sill [*Detrick et al.*, 1987; *Harding et al.*, 1989; *Kent et al.*, 1990] overlying a broader region of the lower crust, with low seismic velocities and few percent of partial melt [*Toomey et al.*, 1990; *Vera et al.*, 1990; *Caress et al.*, 1992]. Along the northern EPR, there is also some evidence for a second magma sill at the Moho [*Garmany*, 1989; *Crawford*, 1995; *Dunn and Toomey*, 1997]. In addition, it has been suggested that the lower crust at the EPR may be composed of a series of gabbroic and partially molten sills [*Boudier et al.*, 1996; *Kelemen et al.*, 1997]. The correlation between MgO content, mantle Bouguer anomaly, and ridge cross-sectional area (Figure 6) implies that higher temperatures in the lower crust correlate with shorter residence times in the midcrustal magma sill. Magmatic events (dike intrusion and eruptions) may thus be closely tied to replenishment of the midcrustal sill from a lower-crustal or subcrustal reservoir [*Kelemen et al.*, 1997; *Natland and Dick*, 1996].

3.2.4 Extrusive layer (2A) thickness. While the magma sill varies considerably in depth, the on-axis layer 2A thickness is relatively constant along the ridge (Figure 9). There is no dependence on spreading rate, and we find no significant difference in the thickness or rate of thickening of the extrusive layer between the northern and southern EPR (Table 1). The high correlation coefficient between on-axis layer 2A thickness and axial depth (Table 2) is due to the uniform value of each of these variables and is not very meaningful. The on-axis thickness of layer 2A is constant for almost the entire range of cross-sectional areas. However, for

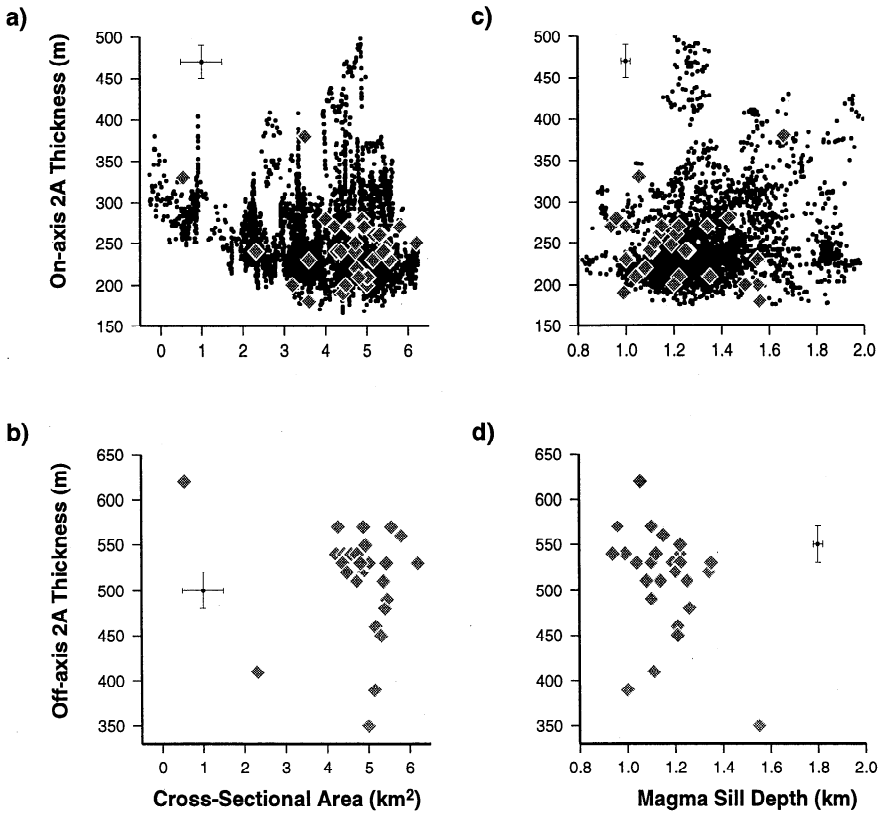

Figure 9. Relationship between indicators of magma budget and layer 2A thickness on- and off-axis. (a) On-axis layer 2A thickness and (b) off-axis layer 2A thickness plotted as a function of cross-sectional area and (c) and (d) as a function of magma sill depth. The symbols and error bar are as in Figure 8. The correlation coefficients for these relationships are given in Table 2. The on-axis layer 2A thickness is uniform except for an increase in thickness where the ridge cross-sectional area is low. The off-axis thickness of layer 2A is not related to morphological indicators of magma supply.

regions with an inferred low magma budget, i.e., deep ridges with small cross-sectional areas, the minimum on-axis layer 2A thickness appears to increase (Figure 9a). Off-axis layer 2A thickness does not relate to cross-sectional area (Figure 9b) and seems to be independent of the magma supply. Both on- and off-axis layer 2A thicknesses are uncorrelated with magma sill depth (Figures 9c and 9d). The width of the zone of across-axis thickening of the extrusive layer shows a large range (0.5 to 4.5 km) (Figure 10), but there is no correlation of the width of extrusive thickening with magma sill width (Figure 10a), and only a weak positive correlation with ridge cross-sectional area (Figure 10b). Extrusive layer thickness thus shows little correlation with either morphological indicators of magma supply or magma sill depth.

3.2.5 Hydrothermal activity. We use measurements of light attenuation in the water column from *Baker and Urabe*

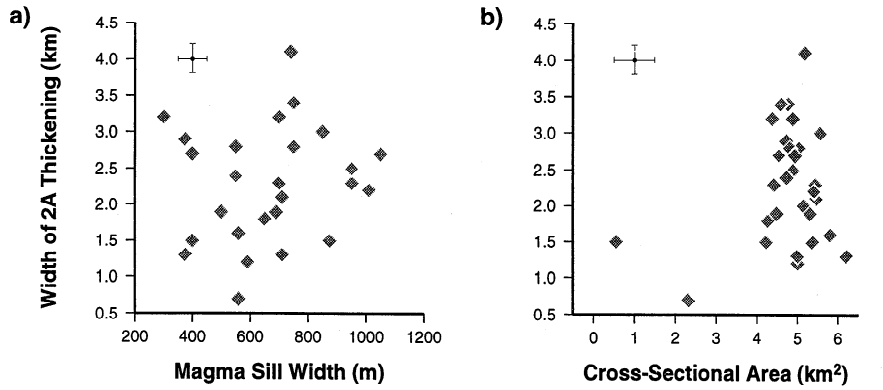

Figure 10. Relationship between the width of the region of thickening of layer 2A, determined from the across-axis seismic lines, and (a) magma sill width and (b) cross-sectional area, both indicators of magmatic budget. The symbols and error bar are as in Figure 8. The correlation coefficients for these relationships are given in Table 2. The width of layer 2A thickening may increase with cross-sectional area.

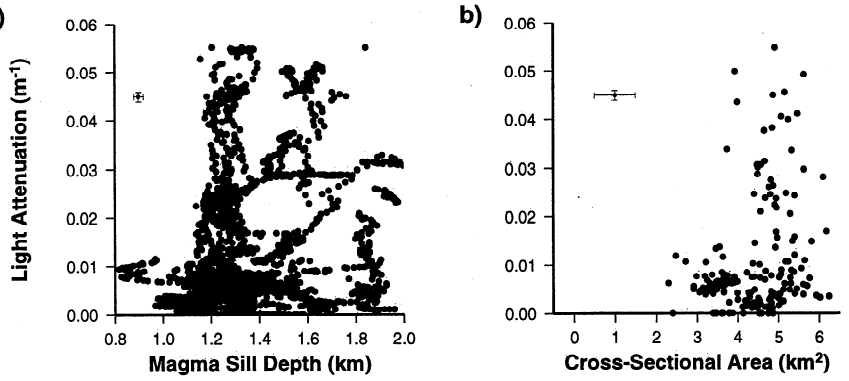

Figure 11. Relationship between light attenuation in the water column, an indicator of hydrothermal venting, and (a) ridge cross-sectional area and (b) magma sill depth along the ridge crest. A generalized error bar is shown. There is little correlation between these parameters.

[1996] to obtain an estimate of the intensity of hydrothermal activity along the ridge axis. Light attenuation is particularly sensitive to the amount of particulate matter in the water column and thus to the presence of high-temperature, black smoker vents. The component of hydrothermal circulation due to diffuse, low-temperature venting is not well recorded in these measurements, but light attenuation measurements do provide a unique coverage for comparison with other regional ridge crest observables. Hydrothermal activity along the SEPR is not strongly correlated with ridge cross-sectional area or magma sill depth (Figure 11). Hydrothermal activity is highly variable along the SEPR and is particularly vigorous from 17°30'S to 18°40'S where the water column survey ended [*Baker and Urabe*, 1996]. The segment centered on 18°30'S shows high venting activity and is unusual in that it does not have an ASC at its summit but rather a summit graben, indicating more extensive tectonic activity. In a study of the distribution of hydrothermal vents along the EPR, *Baker* [1996] concludes that a high magma supply rate and an observable magma sill are necessary but not a guarantee for extensive hydrothermal venting. Our observations suggest that there is a better correlation between hydrothermal venting and regions where an ASC or an axial graben is present [*Lonsdale*, 1989b] than with the presence or depth of the magma lens or with morphological indicators of variations in magma supply (Figure 3).

It is generally thought that hydrothermal fields begin, or are renewed, by dike injection events, which are associated with both heat input and cracking of the shallow crust [*Baker et al.*, 1987; *Haymon et al.*, 1993; *Embley and Chadwick Jr.*, 1994; *Embley et al.*, 1995; *Wright et al.*, 1995] or by the cooling of extremely young lavas [*Fornari and Embley*, 1995]. *Charlou et al.* [1996] and *Auzende et al.* [1996] have observed hydrothermal vent chimneys predominantly located on faults at the edge of axial summit graben in the region from 18°22'S to 18°37'S. In contrast, where the magma sill is unusually shallow, at 17°25'S, they observed mainly diffuse venting of seawater heated by cooling lavas, which are not well recorded using light attenuation measurements. Our observations over the entire region suggest that at the fast spreading SEPR there is always a sufficient heat source near the surface or within the lower crust to drive hydrothermal circulation. However, a permeability structure capable of focusing water migration through the crust is required for longer-lived hydrothermal venting. This permeability structure can be generated by cracking due to recent diking or by tectonic fissuring. The relative importance of these two processes is still unclear.

4. Discussion

From the comparison of axial seismic structure with various indicators of magma supply along the SEPR we find that (1) axial depth, cross-sectional area, and mantle Bouguer anomaly are well correlated with one another and with the along-axis variation in MgO weight percent (Figure 6); (2) magma sill properties (depth and width) are not well-correlated on a regional scale with axial depth, cross-sectional area or MgO weight percent of erupted lavas; (3) on-axis layer 2A thickness is relatively constant and uncorrelated with along-axis variations in cross-sectional area or magma sill depth (Figure 9); and (4) hydrothermal intensity is not strongly correlated with magma sill depth or ridge cross-sectional area (Figure 11). These observations lead to three specific questions regarding the temporal and spatial processes controlling the magmatic construction of the oceanic crust: Why does extrusive thickness not seem to correlate with morphological indicators of magma supply? What controls the depth of the magma sill? Why doesn't magma sill depth correlate with morphological indicators of magma supply?

4.1. Thickness and Construction of the Extrusive Layer

The uniform along-axis thickness of layer 2A (Figure 5a), relative to morphologic indicators of magma supply and to the depth of the magma lens, indicates that construction of the extrusive section is controlled by eruption dynamics rather than magma supply [cf. *Kappus et al.*, 1995]. Models of the emplacement geometry of the extrusive section show that the width of the dike intrusion zone and the length of lava flows control the thickness and thickening rate of layer 2A [e.g., *Kidd*, 1977; *Atwater*, 1979; *Schouten and Denham*, 1979; *Pálmason*, 1980; *Hooft et al.*, 1996]. The relative uniformity of on-axis layer 2A thickness along the ridge axis thus indicates that the dike injection zone has a fairly constant width throughout this region.

Near ridge offsets and along parts of the ridge with small cross-sectional areas, seismic layer 2A thickens (Figure 9a).

Near OSCs the ridge axis is not well localized, and the dike intrusion zone may be wider. This would result in a more distributed dike intrusion and thicker average extrusive section [cf. *Hooft et al.*, 1996]. An alternative possibility is that the magma supply decreases near these ridge offsets, and increased tectonic faulting and fissuring reduces the surficial seismic velocities of the crust. Interpretation of the two-way travel time thicknesses without accounting for these reduced velocities would result in an apparent thickening of seismic layer 2A, which does not correspond to an actual thickening of the extrusive section.

The off-axis thickness and thickening of seismic layer 2A is more variable and may be controlled by the shape of the axial high. Emplacement models predict that if the dikes are rooted in the magma sill, the width of the thickening region of the extrusive section is related to magma sill width. However, our observations show that the width of layer 2A thickening is much greater and more variable than the width of the magma sill (Figure 10a). On the other hand, ridge crest topography does appear to control the construction of layer 2A to some extent. The width of the thickening zone shows a weak positive correlation with ridge cross-sectional area (Figure 10b), a narrower ridge has a narrower zone over which thickening occurs. These observations are consistent with the existence of a narrow dike intrusion zone and lavas that flow a considerable distance off-axis as in the layer 2A construction model of *Hooft et al.* [1996].

4.2. Controls on the Depth of the Magma Sill

It has been suggested that magma ponds at a level of neutral buoyancy (LNB) in the crust where the melt density is equal to the bulk density of the surrounding crust [cf. *Walker*, 1989; *Ryan*, 1993]. We use the composite velocity depth profile of [*Kent et al.*, 1994] as well as a profile incorporating recent results for the shallow crustal velocity structure [*Hussenoeder et al.*, 1996b; *Tolstoy et al.*, 1997] to derive two end-member crustal density profiles [*Christensen and Shaw*, 1970] (Figure 12). Assuming that mid-ocean ridge magma sills are purely molten (density of melt ~2.7±0.02 g/cm^3 [*Hooft and Detrick*, 1993]) the LNB lies at a very shallow depth below the seafloor (200-700 m). As has been previously noted by *Hooft and Detrick* [1993], the depth of the seismically observed magma lens reflector along the SEPR is considerably deeper than this LNB. The median depth of the magma sills along the SEPR is 1300 m below the seafloor, and even the shallowest magma sill (800 m) lies below the LNB. This calculation of the depth of the LNB assumes that the magma sill is completely molten. At 14°10'S on the EPR, nonlinear waveform inversion of wide-aperture seismic reflection data show evidence of near-zero *S* wave velocities in the magma sill [*Singh et al.*, 1996], indicating the presence of pure melt at some locations.

However, other recent studies show that the magma sill sometimes contains a significant proportion of crystals, which will mean that it will be neutrally buoyant at a greater depth. Detailed waveform modeling and amplitude versus offset analysis of multichannel seismic records [*Hussenoeder et al.*, 1996a] show that in some areas along the SEPR the magma sill is able to propagate shear waves, though the shear wave velocity is reduced. Laboratory measurements suggest that these lowered shear wave velocities correspond to a crystal fraction anywhere between 20% and 70% [*Murase and McBirney*, 1973]. Numerical models of the observed compressional wave velocity and anisotropy of the magma sill predict a crystal fraction of 30-50% [*Mainprice*, 1997].

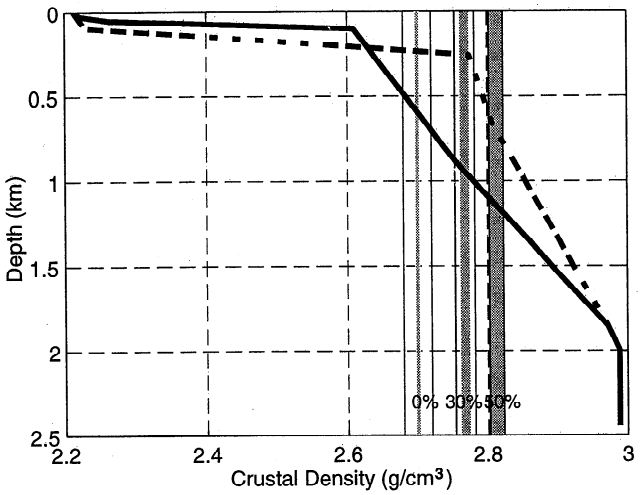

Figure 12. Density structure for the crust, ρ_{crust}, determined from two end-member profiles of compressional wave velocity, V_p, as a function of depth; dark, solid line from *Harding et al.* [1993] and *Vera et al.* [1990]; dark, dashed line from *Hussenoeder et al.* [1996b], *Tolstoy et al.* [1997], and *Vera et al.* [1990]. Velocity is converted to density using the empirical relationship of *Christensen and Shaw* [1970]: $\rho_{crust} = 1.85 + 0.165V_p$. The grey bars indicate the density of a magma with a crystal content of 0%, 30%, and 50%. We assume a linear relationship between the density of the magma sill, ρ_{ms}, and the crystal and melt densities ρ_x and ρ_m, respectively. As a function of the percentage of crystals present, ϕ, the density of the magma sill: $\rho_{ms} = [(100-\phi)/100]\rho_m + \phi/100\rho_x$. Gabbro crystals have densities between 2.90 and 2.95 g/cm^3 [*Christensen and Salisbury*, 1982], the effect of this variability on the magma density is indicated by the width of the grey bars. The effect of the range in melt density (2.7±0.02 g/cm^3 [*Hooft and Detrick*, 1993]) on the density of the magma is shown by the thin dark lines around the grey bars. For a fully molten magma sill the level of neutral buoyancy (LNB) is 200-700 m below the seafloor. As the crystal content increases, the LNB lies deeper in the crust. For high crystalinities (>50%) the observed magma sills may lie at their LNB.

To calculate the density of a magma consisting of both crystals and melt, we assume (1) that magma density is linearly related to the proportions of crystals and melt, (2) that gabbro crystal densities range from ~2.90 to 2.95 g/cm^3 [*Christensen and Salisbury*, 1982], and (3) that basaltic melt density is ~2.7±0.02 g/cm^3 [*Hooft and Detrick*, 1993]. Figure 12 shows bars for the density of a magma with crystal contents of 0%, 30%, and 50%. For a fully molten magma sill the level of neutral buoyancy (LNB) is 200-700 m below the seafloor. As the crystal content increases, the LNB lies deeper in the crust. For high crystalinities (>50%) the observed magma sills may lie at their LNB. Thus magmas sills appear to, in general, lie deeper than their LNB, except when they have high crystal contents or if the melt is quite evolved (i.e., heavier).

Another line of evidence indicating that the magma sills do not pond at a LNB is the large range of magma sill depths observed along the SEPR. Bulk crustal density is closely related to seismic velocity. Since the upper crustal velocity

structure is relatively invariant along the ridge crest [*Tolstoy et al.*, 1997], the upper crustal density profile remains approximately uniform. However, the depth of the seismically observed magma lens reflector varies considerably ranging from 800 to 2000 m below the seafloor (Figure 3). The large variability of magma sill depth observed along the SEPR and its location below the LNB are inconsistent with the hypothesis that the magma lens forms by the ponding of melt at a level of neutral buoyancy within the shallow crust.

We believe that a thermally controlled permeability boundary, such as the solidus horizon, controls the depth of the magma sill at the EPR [*Hooft and Detrick*, 1993; *Phipps Morgan and Chen*, 1993a; *Natland and Dick*, 1996]. The thermal structure of the ridge is a balance between melt supplied to the ridge and heat removed by hydrothermal cooling. If magma ponds at a thermal boundary, the observed variations in magma sill depth are due to changes in axial thermal structure. This concept is consistent with the observed decrease in average depth of the magma sill with increasing spreading rate [*Purdy et al.*, 1992, Table 1].

4.3. Lack of Correlation of the Magma Sill Depth With Indicators of Magma Supply

Models of the thermal balance at mid-ocean ridges show that the advection of heat from variations in melt supply to the ridge affects the crustal thermal structure [*Phipps Morgan and Chen*, 1993b]. Excess heat from an increased magma budget is predicted to result in a shallower magma lens. However, this kind of relationship is inconsistent with the lack of correlation between magma sill depth and cross-sectional area along the SEPR. The large variability in magma sill depth and the lack of correlation with morphologic indicators of magma supply (Figures 5 and 8) require temporal and/or spatial variations in the thermal structure of the ridge that are not solely dependent on spreading rate or magma supply.

We assume that the magma sill lies at the temperature of the solidus (~1200°C). The lower crust is assumed to be relatively isothermal since to satisfy the geophysical observations [*Toomey et al.*, 1990; *Vera et al.*, 1990; *Caress et al.*, 1992], it cannot contain more than a few percent partial melt. The uppermost crust will be rapidly cooled by the circulation of hydrothermal fluids. Temperatures increase rapidly just below the seafloor (0-200°C within the permeable pillow lavas). Temperatures increase more gradually in the sheeted dikes reaching ~400°C at the maximum depth of penetration of hydrothermal fluids [*Alt et al.*, 1986a; *Alt et al.*, 1986b; *Nehlig and Juteau*, 1988; *Gillis and Robinson*, 1990; *Sleep*, 1991]. There is a conductive lid just above the magma sill with very steep thermal gradients, from 400° to 1200°C within a few hundred meters [*Lister*, 1983; *Nicolas*, 1989; *Toomey et al.*, 1994], this is also called the reaction zone [*Alt*, 1995]. Since the magma sill depth ranges from 800 to 2000 m below the seafloor, the steep thermal gradient and the depth of the solidus move up and down considerably within the midcrust to upper crust (Figure 13). Rapid variations in local thermal structure of the upper crust are probably due to an imbalance between the amount of crustal cooling and the heat supplied.

The heat supplied to the magma sill from below is probably relatively invariant; otherwise, the thin sill would quickly be frozen by hydrothermal cooling. Based on the time required to construct the axial high area, along-axis variations in magma supply are probably maintained of order 100,000 years [*Scheirer and Macdonald*, 1993]. Crustal thickness [*Barth and Mutter*, 1996] and abyssal hill characteristics [*Goff*, 1991] also indicate that the average rate of magma supply changes little over several hundred thousand years. A record of the thermal history of axial magma chambers can be deduced from the variations in chemistry of volcanic rocks collected along flow lines on the flanks of the EPR (9°30'N, 10°30'N, and 11°20'N) [*Batiza et al.*, 1996]. These observations show that where the ridge is magmatically robust the magma lens is steady state, and there are no significant changes in eruption temperature over ~800 kyr. On the other hand, in magmatically starved areas, there are large variations in eruption temperature with time (~160°C over 600 kyr), suggesting that the magma lens departs from steady state. These observations are supported by a study of lower crustal rocks exposed in fracture zones and rift deeps along the fast spreading ridge system. Gabbro samples from the ends of segments have more evolved compositions than those from more stable portions of the ridge [*Constantin et al.*, 1996], indicating less frequent replenishment of the magma system. Relative to the more constant supply of melt from below (~100,000 years), the variations in the amount of crustal cooling may depend on the time that has elapsed since a diking event drained the magma sill (one to tens of years, assuming dikes <1 m to several meters wide [*Kidd*, 1977]), as well as on the strength of hydrothermal cooling in the overlying crust (tens to hundreds of years).

The cartoon in Figure 13 summarizes two possible different states of the magma sill for two parts of the ridge that have the same magma budget, i.e., the amount of melt supplied from below is constant. The temperature structures shown are non-steady state thermal profiles resulting from temporal variations in cooling, due to intermittent eruptive and tectonic events at the ridge crest, relative to the constant magma supply from below. In the first case, the crustal permeability is high allowing deep penetration of hydrothermal fluids. The magma lens has also recently erupted onto the seafloor thereby draining away the melt. The amount of heat removed from the magma sill is greater than that being supplied, resulting in a thick conductive lid, and the magma sill lies fairly deep within the crust. This scenario may represent across-axis seismic profile SEPR06 (Figure 4c) where the presence of an axial summit graben enhances the penetration of hydrothermal fluids and there is extensive hydrothermal activity. On the other hand, if the crustal permeability becomes reduced and no eruption has occurred for some time, then the conductive lid will become thin and the magma sill will slowly burn its way to shallower levels in the crust, perhaps by stoping of the overlying sheeted dike section [*Nicolas and Boudier*, 1991]. This scenario is representative of across-axis seismic profile SEPR70 (Figure 4b), where the magma sill lies much shallower than on SEPR06 even though both ridge segments have similar cross-sectional areas, and thus their longer-term magma budgets are the same. The seismic profile in the lower panel of Figure 13 shows apparent local variations in the depth of the magma sill along the ridge axis; a shallow and almost horizontal magma sill fades over a distance of ~7 km giving way to a bright magma sill reflector lying ~1 km deeper.

The relationship between these local, short-term variations in crustal structure and longer-term changes in magma supply to the ridge is shown in an along-axis view in Figure 14. Over

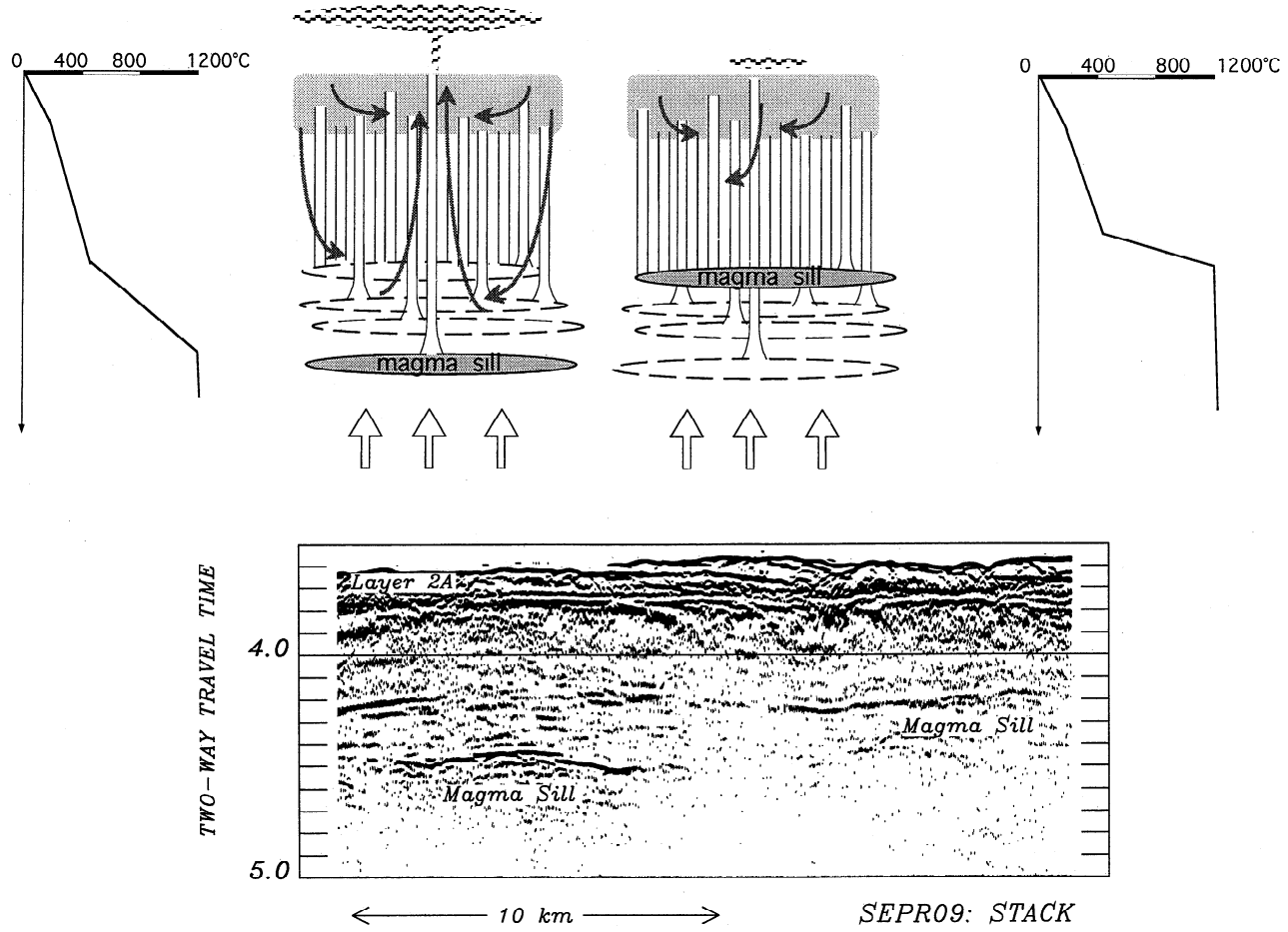

Figure 13. (top) Cartoon showing two ridge crest thermal structures and the accompanying crustal structures: the extrusives and sheeted dikes, the depth of hydrothermal circulation, and the magma sills (see the text for discussion). The two scenarios shown are for a constant magma supply. (left) Heat removal by hydrothermal cooling and the recent eruption of the magma sill exceeds the heat supplied from beneath. The isotherms are moving down in the crust leading to a deeper magma sill and a thick conductive lid. (right) There have been no recent eruptions and hydrothermal cooling is weak. Heat supplied from below exceeds that removed from above, and the magma sill is burning its way up to shallower levels in the crust and is overlain by a thin conductive lid. These scenarios simulate the observations on SEPR06 (Figure 4c) and SEPR70 (Figure 4b), both of which have similar magma budgets, as indicated by their cross-sectional areas. However, on SEPR06 the magma sill is deep and has a weak reflection and there is an axial summit graben with related hydrothermal venting. On the other hand, on SEPR70, the magma sill is shallow and bright and there is no evidence for recent tectonic activity. (bottom) Along-axis seismic section SEPR09 from 18°13'S to 18°02'S illustrating apparent local depth variations of the magma sill. Note how the magma sill is almost horizontal; however, over a distance of ~7 km the shallower magma sill fades giving way to a bright magma sill reflector lying ~1 km deeper.

timescales of ~100,000 years there are variations in magma supply to the different parts of this section of ridge. The resulting variations in cross-sectional area are closely mirrored in the along-axis patterns of the mantle Bouguer anomaly and MgO content of the lavas. However, the magma sill depth, extrusive thickness, and locations of hydrothermal venting show little correlation with these patterns. Changes in average magma sill depth are on a scale of ~200 km. Short-wavelength doming of the magma sill on the scale of ~20 km may be associated with individual volcanic constructs. The extrusive section thickens slightly at the ends of these constructs. The white region around the magma sill indicates a mixed zone of dikes and gabbros generated by rapid (tens to hundreds of years), local changes in the depth of the magma sill (Figure 13). Hydrothermal venting is diffuse where there are recent eruptions and is focused where there is an ASC or axial graben.

5. Summary

We use data from >800 km of the fast spreading SEPR to reexamine the relationship between seismically constrained variations in crustal structure and segment-scale variations in axial depth, morphology, basalt geochemistry, and hydrothermal activity that have often been attributed to along-axis differences in the supply of magma to the ridge. Our main conclusions are as follows:

1. Good correlations exist between axial depth, ridge cross-

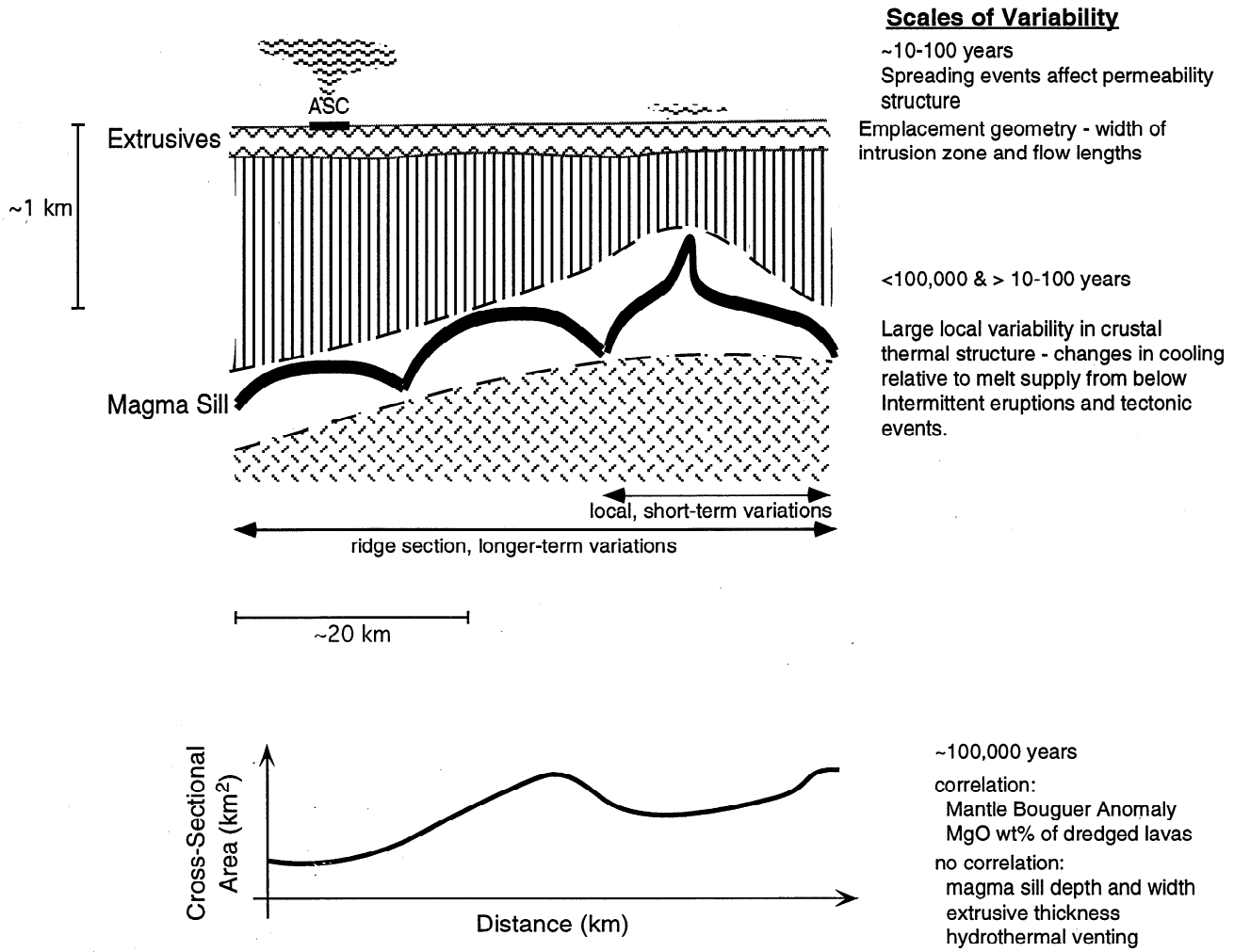

Figure 14. An along-axis view showing the relationship between the local, short-term variations in crustal structure in Figure 13 and longer-term changes in magma supply to the ridge. Approximate horizontal and vertical scales are shown. (top) The gabbro section (hatched pattern), magma sill (thick, double dark line), sheeted dike section (vertical lines), and extrusive section (horizontal zig-zag pattern). The white region around the magma sill indicates a mixed zone of dikes and gabbros generated by short-term depth changes of the magma sill (Figure 13). Hydrothermal venting (wavy pattern) is diffuse where there are recent eruptions (1-10 years), and focused and longer-lived (tens to hundreds of years) where there is an axial summit caldera (ASC). Short-wavelength doming of the magma sill on the scale of ~50 km may be associated with individual volcanic constructs. The extrusive section thickens slightly at the ends of these units. The longer-term changes in average magma sill depth are on a larger scale (~200 km). (bottom) The variation in cross-sectional area along this portion of the ridge axis. General shoaling of the magma sill is accompanied by a trend of increasing cross-sectional area, but in detail the patterns are different.

sectional area, mantle Bouguer anomaly, and the MgO weight percent of basalts recovered from the rise axis. These correlations suggest along-axis variations in lower crustal and upper mantle density which are consistent with variations in magma supply on time scales of ~100,000 years.

2. The magma sill properties (depth and width of the melt lens), seismic layer 2A thickness, and extent of hydrothermal venting are poorly correlated with regional variations in ridge depth and cross-sectional area.

3. The emplacement geometry (width of the intrusion zone, flow lengths), not magma supply, controls extrusive layer (seismic 2A) thickness.

4. Hydrothermal activity is closely linked to spreading events (dike intrusion, eruptions, faulting) which occur on short timescales (about 10-100 years). The presence of a permeability structure that allows water to penetrate to hot rock is key.

5. Magmas accumulate at a depth in the shallow crust where their buoyant ascent is arrested by a thermally controlled permeability boundary.

6. On average, magma sill depth depends on spreading rate and magma supply.

7. We observe a large local variability in magma sill depth (800-2000 m below the seafloor), suggesting that in the short-term the thermal structure of the crust is strongly modified. The advection of heat to the crust by the ascent of melt is relatively continuous. In contrast, the removal of heat from the crust is highly variable and depends on the

variability of hydrothermal cooling, on intermittent eruptive and intrusive episodes that drain the magma sill, and on tectonic events that alter the crustal permeability structure.

Acknowledgments. For the acquisition of the multichannel seismic data we acknowledge the TERA Group (R. Detrick, G. Kent, A. Harding, J. Orcutt, J. Mutter, and P. Buhl). We thank E. Baker, L. Magde, D. Scheirer, and J. Sinton for making their data available to construct the figure synthesizing all the along-axis indicators of magmatic budget (Figure 3). We particularly thank P. Henkart for his help in processing data on the data tape archiving system at the Scripps Institution of Oceanography and for his aid in the use of SIOSEIS. Inspiration came from discussions with J. Escartín and H. Schouten and from discussions during and after a field trip to the Oman ophiolite with P. Kelemen and G. Hirth. We also thank J. Chen (Associate Editor), M.-H. Cormier, and M. Sinha for detailed reviews which greatly helped to improve this manusript. NSF grant OCE-9402033. Woods Hole Oceanographic Institution contribution 9528.

References

Alt, J.C., Subseafloor processes in mid-ocean ridge hydrothermal systems, in *Seafloor Hydrothermal Systems: Physical, Chemical, Biological, and Geological Interactions, Geophys. Monogr. Ser.*, vol. 91, edited by S.E. Humphris et al., pp. 85-114, AGU, Washington, D. C., 1995.

Alt, J.C., J. Honnorez, C. Laverne, and R. Emmermann, Hydrothermal alteration of a 1 km section through the upper oceanic crust, Deep Sea Drilling Project Hole 504B: The mineralogy, chemistry, and evolution of seawater-basalt interactions, *J. Geophys. Res.*, *91*, 10,309-10,335, 1986a.

Alt, J.C., K. Muehlenbachs, and J. Honnorez, An oxygen isotopic profile through the upper kilometer of oceanic crust, Deep Sea Drilling Project Hole 504B, *Earth Planet. Sci. Lett.*, *80*, 217-229, 1986b.

Atwater, T., Constraints from the FAMOUS area concerning the structure of the oceanic section, in *Deep Drilling Results in the Atlantic Ocean: Ocean Crust, Maurice Ewing Ser.*, vol. 2, edited by M. Talwani, C.G. Harrison, and D.E. Hayes, pp. 33-42, AGU, Washington, D. C., 1979.

Auzende, J.-M. et al., Recent tectonic, magmatic, and hydrothermal activity on the East Pacific Rise between 17°S and 19°S: Submersible observations, *J. Geophys. Res.*, *101*, 17,995-18,010, 1996.

Baker, E.T., Geological indexes of hydrothermal venting, *J. Geophys. Res.*, *101*, 13,741-13,753, 1996.

Baker, E.T., and T. Urabe, Extensive distribution of hydrothermal plumes along the superfast spreading East Pacific Rise. 13°30'-18°40'S, *J. Geophys. Res.*, *101*, 8685-8695, 1996.

Baker, E.T., G.J. Massoth, and R.A. Feely, Cataclysmic hydrothermal venting on the Juan de Fuca Ridge, *Nature*, *329*, 149-151, 1987.

Barth, G.A., and J.C. Mutter, Variability in oceanic crustal thickness and structure: Multichannel seismic reflection results from the northern East Pacific Rise, *J. Geophys. Res.*, *101*, 17951-17975, 1996.

Batiza, R., Y. Niu, J.L. Karsten, W. Boger, E. Potts, L. Norby, and R. Butler, Steady and non-steady state magma chambers below the East Pacific Rise, *Geophys. Res. Lett.*, *23*, 221-224, 1996.

Begnaud, M.L., J.S. McClain, G.A. Barth, J.A. Orcutt, and A.J. Harding, Velocity structure from forward modeling of the eastern ridge-transform intersection area of the Clipperton Fracture Zone, East Pacific Rise, *J. Geophys. Res.*, *102*, 7803-7820, 1997.

Boudier, F., A. Nicolas, and B. Ildefonse, Magma chambers in the Oman ophiolite: Fed from the top or from the bottom?, *Earth Planet. Sci. Lett.*, *144*, 239-250, 1996.

Brysk, H., Numerical analysis of the 45° finite-difference equation for migration, *Geophysics*, *48*, 532-542, 1983.

Carbotte, S., J.C. Mutter, and L. Xu, Contribution of volcanism and tectonism to axial and flank morphology of the southern East Pacific Rise, 17°10'-17°40'S, from a study of layer 2A geometry, *J. Geophys. Res.*, *102*, 10,165-10,184, 1997.

Caress, D., M. Burnett, and J. Orcutt, Tomographic image of the axial low velocity zone at 12°50'N on the East Pacific Rise, *J. Geophys. Res.*, *97*, 9243-9264, 1992.

Charlou, J.L., Y. Fouquet, J.P. Donval, J.M. Auzende, P. Jean-Baptiste, M. Stievenard, and S. Michel, Mineral and gas chemistry of hydrothermal fluids on an ultrafast spreading ridge: East Pacific Rise, 17° to 19°S (Naudur cruise, 1993) phase separation processes controlled by volcanic and tectonic activity, *J. Geophys. Res.*, *101*, 15,899-15,919, 1996.

Christensen, N.I., and M.H. Salisbury, Lateral heterogeneity in the seismic structure of the oceanic crust inferred from velocity studies in the Bay of Islands ophiolites, Newfoundland, *Geophys. J. R. Astron. Soc.*, *68*, 675-688, 1982.

Christensen, N.I., and G.H. Shaw, Elasticity of mafic rocks from the Mid-Atlantic Ridge, *Geophys. J. R. Astron. Soc.*, *20*, 271-284, 1970.

Christeson, G.L., Seismic constraints on shallow crustal processes at the East Pacific Rise, Ph.D. thesis, Mass. Inst. of Technol./Woods Hole Oceanogr. Inst. Joint Program in Oceanography, Woods Hole, Mass., 1994.

Christeson, G.L., G.M. Purdy, and G.J. Fryer, Structure of young upper crust at the East Pacific Rise near 9°30'N, *Geophys. Res. Lett.*, *19*, 1045-1048, 1992.

Collier, J., and M. Sinha, Seismic images of a magma chamber beneath the Lau Basin back-arc spreading centre, *Nature*, *346*, 646-648, 1990.

Collier, J.S., and M.C. Sinha, Seismic mapping of a magma chamber beneath the Valu Fa Ridge, Lau Basin, *J. Geophys. Res.*, *97*, 14,031-14,054, 1992.

Constantin, M., R. Hekinian, D. Bideau, and R. Hébert, Construction of the oceanic lithosphere by magmatic intrusions: Petrological evidence from plutonic rocks formed along the fast-spreading East Pacific Rise, *Geology*, *24*, 731-734, 1996.

Cormier, M.-H., and K.C. Macdonald, A three-dimensional gravity analysis of the East Pacific Rise from 18° to 21°30'S, *J. Geophys. Res.*, *100*, 8063-8082, 1995.

Crawford, W.C., Low shear velocity zones within the East Pacific Rise at 9°48'N, *Eos Trans. AGU, 76 (46)*, Fall Meet. Suppl., F401, 1995.

Davis, A.S., D.A. Clague, and J.L. Morton, Volcanic glass compositions from two spreading centers in the Lau Basin, south-west Pacific, *Geol. Jahrb., Reihe D*, *72*, 481-501, 1991.

DeMets, C., R.G. Gordon, D.F. Argus, and S. Stein, Effect of recent revision to the geomagnetic reversal time scale on estimates of current plate motions, *Geophys. Res. Lett.*, *21*, 2192-2194, 1994.

Detrick, R.S., P. Buhl, E.E. Vera, J.C. Mutter, J.A. Orcutt, J.A. Madsen, and T.M. Brocher, Multichannel seismic imaging of a crustal magma chamber along the East Pacific Rise, *Nature*, *326*, 35-41, 1987.

Detrick, R.S., A.J. Harding, G.M. Kent, J.A. Orcutt, J.C. Mutter, and P. Buhl, Seismic structure of the southern East Pacific Rise, *Science*, *259*, 499-503, 1993.

Dunn, R.A., and D.R. Toomey, Seismological evidence for three-dimensional melt migration beneath the East Pacific Rise, *Nature*, *388*, 259-262, 1997.

Embley, R.W., and W.W. Chadwick Jr., Volcanic and hydrothermal processes associated with a recent phase of seafloor spreading at the northern Cleft segment: Juan de Fuca Ridge, *J. Geophys. Res.*, *99*, 4741-4760, 1994.

Embley, R.W., W.W. Chadwick, J.I.R. Jonasson, D.A. Butterfield, and E.T. Baker, Initial results of the rapid response to the 1993 CoAxial event: Relationships between hydrothermal and volcanic processes, *Geophys. Res. Lett.*, *22*, 143-146, 1995.

Fornari, D.J., and R.W. Embley, Tectonic and volcanic controls on hydrothermal processes at the mid-ocean ridge: An overview based on near-bottom and submersible studies, in *Seafloor Hydrothermal Systems: Physical, Chemical, Biological, and Geological Interactions, Geophys. Monogr. Ser.*, vol. 91, edited by S.E. Humphris et al., pp. 1-46, AGU, Washington, D. C., 1995.

Fresnel, G., R. Mühe, and P. Stoffa, Petrology of the volcanic rocks from the Lau Basin, southwest Pacific, *Geol. Jahrb., Reihe D*, *72*, 396-480, 1991.

Garmany, J., Accumulations of melt at the base of young oceanic crust, *Nature*, *340*, 628-632, 1989.

Gillis, K.M., and P.T. Robinson, Patterns and processes of alteration in the lavas and dikes of the Troodos ophiolite, Cyprus, *J. Geophys. Res.*, *95*, 21,523-21,548, 1990.

Goff, J.A., A global and regional stochastic analysis of near-ridge abyssal hill morphology, *J. Geophys. Res.*, *96*, 21,713-21,737, 1991.

Harding, A.J., J.A. Orcutt, M.E. Kappus, E.E. Vera, J.C. Mutter, P. Buhl, R.S. Detrick, and T. Brocher, Structure of young oceanic crust at 13°N on the East Pacific Rise from expanding spread profiles, *J. Geophys. Res.*, *94*, 12,163-12,196, 1989.

Harding, A.J., G.M. Kent, and J.A. Orcutt, A multichannel seismic investigation of the upper crustal structure at 9°N on the East Pacific Rise: Implications for crustal accretion, *J. Geophys. Res.*, *98*, 13,925-13,944, 1993.

Haymon, R.M., D.J. Fornari, M.H. Edwards, S. Carbotte, D. Wright, and K.C. Macdonald, Hydrothermal vent distribution along the East Pacific Rise crest (9°09'-54'N) and its relationship to magmatic and tectonic processes on fast-spreading mid-ocean ridges, *Earth Planet. Sci. Lett.*, *104*, 513-534, 1991.

Haymon, R.M. et al., Volcanic eruption of the mid-ocean ridge along the East Pacific Rise crest at 9°45'-52'N: Direct submersible observations of seafloor phenomena associated with an eruption event in April, 1991, *Earth Planet. Sci. Lett.*, *119*, 85-101, 1993.

Herron, T.J., Lava flow layer-East Pacific Rise, *Geophys. Res. Lett.*, *9*, 17-20, 1982.

Hooft, E.E., and R.S. Detrick, The role of density in the accumulation of basaltic melts at mid-ocean ridges, *Geophys. Res. Lett.*, *20*, 423-426, 1993.

Hooft, E.E.E., H. Schouten, and R.S. Detrick, Constraining crustal emplacement processes from the variation of seismic layer 2A thickness at the East Pacific Rise, *Earth Planet. Sci. Lett.*, *142*, 289-309, 1996.

Hussenoeder, S.A., J.A. Collins, G.M. Kent, R.S. Detrick, and the TERA Group, Seismic analysis of the axial magma chamber reflector along the southern East Pacific Rise from conventional reflection profiling, *J. Geophys. Res.*, *101*, 22,087-22,105, 1996a.

Hussenoeder, S.A., R.S. Detrick, G.M. Kent, and A. Harding, A comparison of upper crustal structure between fast and slow spreading ridges from genetic algorithm seismic waveform inversion, *Eos Trans. AGU, 77 (46)*, Fall Meet. Suppl., F729, 1996b.

Kappus, M.E., A.J. Harding, and J.A. Orcutt, A baseline for upper crustal seismic velocity variations along the East Pacific Rise at 13°N, *J. Geophys. Res.*, *100*, 6143-6161, 1995.

Kelemen, P.B., K. Koga, and N. Shimizu, Geochemistry of gabbro sills in the crust/mantle transition zone of the Oman ophiolite: Implications for the origin of the oceanic lower crust, *Earth Planet. Sci. Lett.*, *146*, 475-488, 1997.

Kent, G.M., A.J. Harding, and J.A. Orcutt, Evidence for a smaller magma chamber beneath the East Pacific Rise at 9°30'N, *Nature*, *344*, 650-653, 1990.

Kent, G.M., A.J. Harding, and J. Orcutt, Distribution of magma beneath the East Pacific Rise near the 9°03'N overlapping spreading center from forward modeling of common depth point data, *J. Geophys. Res.*, *98*, 13,971-13,996, 1993a.

Kent, G.M., A.J. Harding, and J.A. Orcutt, Distribution of magma beneath the East Pacific Rise between the Clipperton Transform and the 9°17'N Deval from forward modeling of common depth point data, *J. Geophys. Res.*, *98*, 13,945-13,969, 1993b.

Kent, G.M., A.J. Harding, J.A. Orcutt, R.S. Detrick, J.C. Mutter, and P. Buhl, Uniform accretion of oceanic crust south of the Garrett Transform at 14°15'S on the East Pacific Rise, *J. Geophys. Res.*, *99*, 9097-9116, 1994.

Kidd, R.G.W., A model for the process of formation of the upper oceanic crust, *Geophys. J. R. Astron. Soc.*, *50*, 149-183, 1977.

Langmuir, C.H., J.F. Bender, and R. Batiza, Petrologic and tectonic segmentation of the East Pacific Rise, 5°30'-14°30'N, *Nature*, *322*, 422-429, 1986.

Liner, C.L., General theory and antaomy of dip-moveout, *Geophysics*, *55*, 595-607, 1990.

Lister, C.R.B., On the intermittency and crystallization mechanisms of sub-seafloor magma chambers, *Geophys. J. R. Astron. Soc.*, *73*, 351-365, 1983.

Lonsdale, P., Overlapping rift zones at the 5.5°S offset of the East Pacific Rise, *J. Geophys. Res.*, *88*, 9393-9406, 1983.

Lonsdale, P., Comments on "East Pacific Rise from Siqueiros to Orozco Fracture Zones: Along-strike continuity of the axial neovolcanic zone and structure and evolution of overlapping spreading centers" by K. Macdonald, J. Sempéré, and P.J. Fox, *J. Geophys. Res.*, *91*, 10,493-10,499, 1986.

Lonsdale, P., The rise flank trails left by migrating offsets of the equatorial Ewast Pacific Rise axis, *J. Geophys. Res.*, *94*, 713-743, 1989a.

Lonsdale, P., Segmentation of the Pacific-Nazca Spreading Center, 1°N-20°S, *J. Geophys. Res.*, *94*, 12,197-12,225, 1989b.

Macdonald, K.C., and P.J. Fox, The axial summit graben and cross-sectional shape of the East Pacific Rise as indicators of axial magma chambers and recent volcanic eruptions, *Earth Planet. Sci. Lett.*, *88*, 119-131, 1988.

Macdonald, K.C., J.-C. Sempéré, and P.J. Fox, East Pacific Rise from Siquciros to Orozco fracture zones: Along-strike continuity of axial neovolcanic zones and structure and evolution of overlapping spreading centers, *J. Geophys. Res.*, *89*, 6049-6069, 1984.

Macdonald, K. et al., The East Pacific Rise and its flanks 8-18°N: History of segmentation, propagation and spreading direction based on SeaMARC II and Sea Beam studies, *Mar. Geophys. Res.*, *14*, 299-344, 1992.

Madsen, J.A., R.S. Detrick, J.C. Mutter, P. Buhl, and J.C. Orcutt, A two- and three-dimensional analysis of gravity anomalies associated with the East Pacific Rise at 9°N and 13°N, *J. Geophys. Res.*, *95*, 4967-4987, 1990.

Magde, L.S., R.S. Detrick, and the TERA Group, Crustal and upper mantle contribution to the axial gravity anomaly at the southern East Pacific Rise, *J. Geophys. Res.*, *100*, 3747-3766, 1995.

Mahoney, J.J., J.M. Sinton, M.D. Kurz, J.D. Macdougall, K.J. Spencer, and G.W. Lugmair, Isotope and trace element characteristics of a super-fast spreading ridge: East Pacific Rise, 13-23°S, *Earth Planet. Sci. Lett.*, *121*, 173-193, 1994.

Mainprice, D., Modeling the anisotropic seismic properties of partially molten rocks found at mid-ocean ridges, *Tectonophysics*, *279*, 161-179, 1997.

Murase, T., and A. McBirney, Properties of some common igneous rocks and their melts at high temperatures, *Geol. Soc. Am. Bull.*, *84*, 3563-3592, 1973.

Mutter, J.C., S.M. Carbotte, W. Su, L. Xu, P. Buhl, R.S. Detrick, G.M. Kent, J.A. Orcutt, and A.J. Harding, Seismic images of active magma systems beneath the East Pacific Rise between 17°05' and 17°35'S, *Science*, *268*, 391-395, 1995.

Natland, J.H., and H.J.B. Dick, Melt migration through high-level gabbroic cumulates of the East Pacific Rise at Hess Deep: The origin of magma lenses and the deep crustal structure of fast-spreading ridges, *Proc. Ocean Drill. Program Sci. Results*, *147*, 21-58, 1996.

Nehlig, P., and T. Juteau, Flow porosities, permeabilities and preliminary data on fluid inclusions and fossil thermal gradients in the crustal sequence of the Sumail ophiolite (Oman), *Tectonophysics*, *151*, 199-221, 1988.

Nicolas, A., *Structure of Ophiolites and Dynamics of Oceanic Lithosphere*, vol. 4, 367 pp., Kluwer Acad., Norwell, Mass., 1989.

Nicolas, A., and F. Boudier, Rooting of the sheeted dike complex in the Oman ophiolite, in *Ophiolite Genesis and Evolution of the Oceanic Lithosphere*, edited by T. Peters, A. Nicolas, and R. Coleman, pp. 39-54, Minist. of Pet. and Miner., Muscat, Oman, 1991.

Nicolas, A., F. Boudier, and B. Ildefonse, Variable crustal thickness in the Oman ophiolite: Implications for oceanic crust, *J. Geophys. Res.*, *101*, 17941-17950, 1996.

Pálmason, G., Continuum model of crustal generation in Iceland: Kinematic aspects, *J. Geophys.*, *47*, 7-18, 1980.

Phipps Morgan, J., and Y.J. Chen, The genesis of oceanic crust: Magma injection, hydrothermal circulation, and crustal flow, *J. Geophys. Res.*, *98*, 6283-6298, 1993a.

Phipps Morgan, J., and Y.J. Chen, Dependence of ridge-axis morphology on magma supply and spreading rate, *Nature*, *364*, 706-708, 1993b.

Posiolova, L.V., H. van Avendonk, A.J. Harding, and J.A. Orcutt, Seismic refraction observations from the western and central portions of the Clipperton Transform Fault, East Pacific Rise, *Eos Trans. AGU, 76 (46)*, Fall Meet. Suppl., F597, 1995.

Purdy, G.M., G. Christeson, and S. Solomon, Relationship between spreading rate and the seismic structure of mid-ocean ridges, *Nature*, *355*, 815-817, 1992.

Ryan, M.P., Neutral buoyancy and the structure of mid-ocean ridge magma reservoirs, *J. Geophys. Res.*, *98*, 22,321-22,338, 1993.

Scheirer, D.S., and K.C. Macdonald, Variation in cross-sectional area of the axial ridge along the East Pacific Rise: Evidence for the magmatic budget of a fast spreading center, *J. Geophys. Res.*, *98*, 7871-7886, 1993.

Schouten, H., and C.R. Denham, Modeling the oceanic magnetic source layer, in *Deep Drilling Results in the Atlantic Ocean: Ocean Crust, Maurice Ewing Ser.*, vol. 2, edited by M. Talwani, C.G. Harrison, and D.E. Hayes, pp. 151-159, AGU, Washington, D. C., 1979.

Singh, S., G. Kent, A. Harding, and J. Orcutt, *P*- and *S*-wave velocity structure of the upper crust at 14°10'S East Pacific Rise from waveform inversion, *Eos Trans. AGU, 77 (46)*, Fall Meet. Suppl., F664, 1996.

Sinha, M.C., Segmentation and rift propagation at the Valu Fa ridge, Lau

Basin: Evidence from gravity data, *J. Geophys. Res.*, *100*, 15,025-15,043, 1995.

Sinton, J.M., S.M. Smaglik, J.J. Mahoney, and K.C. Macdonald, Magmatic processes at superfast spreading mid-ocean ridges: Glass compositional variations along the East Pacific Rise 13°S-23°S, *J. Geophys. Res.*, *96*, 6133-6155, 1991.

Sisson, T.W., and T.L. Grove, Temperatures and H_2O contents of low-MgO high-alumina basalts, *Contrib. Mineral. Petrol.*, *113*, 167-184, 1993.

Sleep, N.H., Hydrothermal circulation, Anhydrite precipitation, and thermal structure at ridge axes, *J. Geophys. Res.*, *96*, 2375-2387, 1991.

Tighe, S.A., R.S. Detrick, P.J. Fox, C.H. Langmuir, J.C. Mutter, W.B. Ryan, and R.C. Tyce, East Pacific Rise data synthesis final report, vol. 1, edited by S.A. Tighe, JOI, Washington, D. C., 1988.

Tolstoy, M., A.J. Harding, J.A. Orcutt, and the TERA Group, Deepening of the axial magma chamber on the southern East Pacific Rise toward the Garrett Fracture Zone, *J. Geophys. Res.*, *102*, 3097-3108, 1997.

Toomey, D.R., G.M. Purdy, S.C. Solomon, and W.S.D. Wilcock, The three-dimensional seismic velocity structure of the East Pacific Rise near latitude 9°30'N, *Nature*, *347*, 639-645, 1990.

Toomey, D.R., S.C. Solomon, and G.M. Purdy, Tomographic imaging of the shallow crustal structure of the East Pacific Rise at 9°320'N, *J. Geophys. Res.*, *99*, 24,135-24,157, 1994.

Vera, E.E., J.C. Mutter, P. Buhl, J.A. Orcutt, A.J. Harding, M.E. Kappus, R.S. Detrick, and T.M. Brocher, The structure of 0 to 0.2 m.y.-old oceanic crust at 9°N on the East Pacific Rise from expanded spread profiles, *J. Geophys. Res.*, *95*, 15,529-15,556, 1990.

Walker, G.P.L., Gravitational (density) controls on volcanism, magma chambers and intrusions, *Austr. J. Earth Sci.*, *36*, 149-165, 1989.

Wang, X., and J.R. Cochran, Gravity anomalies, isostasy, and mantle flow at the East Pacific Rise crest, *J. Geophys. Res.*, *98*, 19,505-19,532, 1993.

Wang, X., J.R. Cochran, and G. Barth, Gravity anomalies, crustal thickness and the pattern of mantle flow at the fast spreading East Pacific Rise, 9°N-10°N: Evidence for three-dimensional upwelling, *J. Geophys. Res.*, *101*, 17,927-17,940, 1996.

Weidicke, M., and J. Collier, Morphology of the Valu Fa spreading ridge in the southern Lau Basin, *J. Geophys. Res.*, *98*, 11769-11782, 1993.

Wilson, D., Focused mantle upwelling beneath mid-ocean ridges: Evidence from seamount formation and isostatic compensation of topography, *Earth Planet. Sci. Lett.*, *113*, 41-55, 1992.

Wright, D.J., R.M. Haymon, and D.J. Fornari, Crustal fissuring and its relationship to magmatic and hydrothermal processes on the East Pacific Rise crest (9°12' to 54'N), *J. Geophys. Res.*, *100*, 6097-6120, 1995.

R.S. Detrick, Department of Geology and Geophysics, Woods Hole Oceanographic Institution, Woods Hole, MA 02543. (e-mail: rdetrick@whoi.edu)

E.E.E. Hooft, Department of Terrestrial Magnetism, Carnegie Institution of Washington, Washington, D.C. 20015. (e-mail: ehooft@whoi.edu)

G.M. Kent, Institute of Geophysics and Planetary Physics, Scripps Institution of Oceanography, La Jolla, CA 92037.

(Received September 23, 1996; revised July 31, 1997; accepted August 8, 1997.)